Information Fusion Strategies for Collaborative Inertial Radio SLAM

Joshua J. Morales, *Member, IEEE*, Joe J. Khalife, *Student Member, IEEE*, and Zaher M. Kassas, *Senior Member, IEEE*

***Abstract*— Information fusion strategies for vehicles navigating while aiding their inertial navigation systems (INSs) with terrestrial signals of opportunity (SOPs) are developed and studied. The following problem is considered. Multiple navigating vehicles with access to global navigation satellite system (GNSS) signals are aiding their on-board INSs with GNSS pseudoranges. While navigating, vehicle-mounted receivers draw pseudorange measurements from terrestrial SOPs (e.g., AM/FM radio, digital television, cellular) with unknown emitter positions and unknown and unsynchronized clocks. The vehicles share INS data and SOP pseudoranges to collaboratively estimate the SOPs' states through an extended Kalman filter using tight coupling. After some time, GNSS signals become unavailable, at which point the navigating vehicles use shared INS and SOP information to continue navigating in a collaborative inertial radio simultaneous localization and mapping (CIRSLAM) framework. This paper develops such CIRSLAM framework and synthesizes what SOP and INS information should be shared between collaborators. Two information fusion strategies are compared: 1) sharing time-of-arrival (TOA) measurements from SOPs; 2) sharing time-difference-of-arrival (TDOA) measurements taken with reference to an SOP. Next, a strategy to efficiently share INS information along with SOP information is discussed. Monte Carlo simulation results are presented that support the analytical findings that vehicles navigating in a CIRSLAM framework, while sharing and fusing SOP TOA measurements, produce a smaller or equal estimation error covariance compared to fusing SOP TDOA measurements. Experimental results are presented demonstrating two unmanned aerial vehicles (UAVs) navigating in a CIRSLAM framework with SOP TOA measurements from terrestrial cellular towers. The final UAVs' localization error after 30 seconds of GPS unavailability were reduced compared to using an INS alone from around 55 m to around 6 m.**

***Index Terms*— Autonomous vehicles, navigation, localization, INS, signals of opportunity, collaborative navigation, information fusion, GNSS, GPS, TOA, TDOA, SLAM.**

Manuscript received 29 August 2020; revised 17 June 2021 and 29 July 2021; accepted 1 October 2021. Date of publication 18 November 2021; date of current version 9 August 2022. This work was supported in part by the Office of Naval Research (ONR) under Grant N00014-19-1-2511 and in part by the National Science Foundation (NSF) under Grant 1929965 and Grant 1929571. The Associate Editor for this article was G. Mao. *(Corresponding author: Zaher M. Kassas.)*

Joshua J. Morales was with University of California, Irvine, CA 92697 USA. He is now with StarNav LLC, Riverside, CA 92501 USA (e-mail: joshua.morales@ieee.org).

Joe J. Khalife is with the Department of Electrical Engineering and Computer Science (EECS), University of California, Irvine, CA 92697 USA (e-mail: khalifej@uci.edu).

Zaher M. Kassas is with the Department of Mechanical and Aerospace Engineering, University of California, Irvine, CA 92697 USA (e-mail: zkassas@ieee.org).

This article has supplementary downloadable material available at https://doi.org/10.1109/TITS.2021.3118678, provided by the authors.

Digital Object Identifier 10.1109/TITS.2021.3118678

I. Introduction

THE last decade has seen a dramatic increase in the research and development of semi- and fully-autonomous vehicles. In 2019 alone, the private sector saw record-breaking investments to develop self-driving cars, autonomous package delivery robots, unmanned aerial vehicles (UAVs), and other autonomous vehicles of-the-like [1]. Besides the private sector, the U.S. Department of Defense requested $9.39 billion in 2019 for unmanned systems and associated technologies [2]. As these autonomous vehicles begin to operate alongside human-operated vehicles, requirements on their navigation system's robustness and accuracy of their position, velocity, and time solution become extremely stringent [3], [4]. To meet such stringent requirements, vehicular navigation systems must draw and fuse information from various sensing modalities and, if available, other vehicles in their vicinity. Fortunately, advances of autonomous features on automobiles have driven the development of vehicle-to-vehicle (V2V) communication technologies. These technologies enable current and future vehicles to share information with other vehicles, which improve situational awareness and navigation performance.

Today's navigation systems fuse absolute positioning information from a global navigation satellite system (GNSS) receiver with dead reckoning information from an inertial navigation system (INS) [5], and potentially a multitude of other information sources [6] (e.g., lidar [7]–[9], cameras [10]–[12], and maps [13]–[15]). Relying on GNSS alone to provide absolute positioning poses an alarming vulnerability: GNSS signals could become unavailable or unreliable in environments such as deep urban canyons or environments experiencing a malicious attack (e.g., jamming or spoofing). During prolonged periods without absolute position information from GNSS, the errors in the INS (and other dead-reckoning-type sensors) will inevitably diverge, compromising the vehicle's accurate and safe operation. These vulnerabilities have prompted the U.S. Department of Transportation to emphasize that there is a need for positioning technologies that can work in the absence of GPS [16].

Signals of opportunity (SOPs) have been demonstrated as an attractive source of absolute positioning information in the absence of GNSS signals [17]. SOPs are ambient radio frequency signals that are not intended for navigation, such as AM/FM radio [18], [19], cellular [20]–[23], digital television [24], [25], and low Earth orbit (LEO) satellite signals [26], [27]. With appropriately designed receivers and algorithms, SOPs may be exploited for standalone navigation

[23], [28] or as an aiding source for an INS [29], [30]. This paper considers using SOPs to provide aiding corrections in a tightly-coupled aided INS.

SOPs posses several desirable characteristics for vehicular navigation: (i) ubiquity in most environments of interest, (ii) signal diversity in frequency and direction, (iii) signal reception with carrier-to-noise ratio that is often tens of decibels (dBs) higher than that of GNSS signals, (iv) free to use with SOP navigation receivers that do not require network subscriptions, and (v) no deployment cost, since their infrastructure is already operational and maintained by service providers. Even if GNSS pseudoranges are reliable, adding terrestrial SOP pseudorange measurements to the navigation filter will significantly reduce positioning errors for land, sea, and air vehicles. This is primarily due to a reduction in the vertical dilution of precision (VDOP), which is achieved when terrestrial SOP pseudoranges, which have small elevation angles, are used with GNSS pseudoranges, which inherently have larger elevation angles [31]. Even if very accurate GNSS real-time kinematic (RTK) positioning is being used, introducing an additional radio signal with positioning information increases reliability in case the GNSS radio link becomes jammed, which would render RTK unusable. However, unlike GNSS, whose satellites' states are known via their transmitted navigation message, the states of SOPs, namely their position and clock states, are typically unknown *a priori* and must be estimated [32].

To address this estimation problem, this paper develops a collaborative inertial radio simultaneous localization and mapping (CIRSLAM) framework, in which multiple vehicles estimate the *unknown* states of terrestrial SOPs along with the states of navigating vehicles using shared SOP and INS information. Single vehicle inertial radio SLAM with *terrestrial* SOPs was studied in [30], [33]. Radio SLAM is similar to the SLAM problem in robotics [34]. However, in contrast to the *static* states associated with traditional SLAM landmarks (e.g., buildings, light poles, trees, etc.) the radio SLAM map is more complex, as it is composed of both (i) static and (ii) *stochastic and dynamic* states, which correspond to the SOP emitter positions and clock error states (bias and drift), respectively. Radio SLAM provides an absolute position source for INS aiding in the absence of GNSS signals, preventing INS drift during prolonged periods of GNSS unavailability.

In extended Kalman filter (EKF)-based CIRSLAM, collaborating vehicles can improve their state estimates over single-vehicle inertial radio SLAM by sharing and fusing mutual measurements made on SOPs along with the vehicles' INS information [35]. This paper addresses two practical and theoretical issues to determine how to extract the most information from shared SOP measurements. First, the estimation uncertainties of two information fusion strategies in a CIRSLAM framework are compared: (i) time-of-arrival (TOA) and (ii) time-difference-of-arrival (TDOA) taken with reference to a selected SOP. Second, an efficient method to package and communicate INS and SOP information is developed.

Terrestrial SOP-based navigation with TDOA measurements is similar to navigation with Loran- both are hyperbolic positioning approaches, except SOPs enjoy the aforementioned desirable characteristics, i.e., geometric diversity (many towers), free infrastructure, and diversity in frequency. However, SOPs come with the additional challenge of having unknown positions. This challenge is addressed in this paper, complete with sufficient information for the interested reader to implement an EKF-based CIRSLAM filter.

The remainder of this paper is organized as follows. Section II surveys related research on TOA versus TDOA positioning and maintaining inter-vehicle correlations. Section III provides a high-level description of the information fusion strategies that this article studies. Section IV describes the dynamics model of the SOPs and navigating vehicles as well as the receivers' measurement model. Section V describes the EKF-based CIRSLAM framework, an efficient method to communicate INS and SOP information between collaborators, and the TOA and TDOA information fusion strategies. Section VI compares the estimation performance of each fusion strategy. Section VII discusses the simulation environment and presents simulation results comparing the estimation performance of the TOA and TDOA information fusion strategies. Section VIII presents experimental results of collaborating UAVs using cellular SOPs to aid their INSs. Section IX concludes this paper by summarizing the developed theory, algorithms, and experimental results.

II. Related Work

The use of TOA and TDOA for positioning has been studied in different contexts. In [36], it was determined that using GPS pseudoranges as TOA and TDOA produced identical positioning results. In [37], the Cramér-Rao lower bound (CRLB) was shown to be identical for receivers with *known states* that are using either TOA or TDOA to localize multiple transmitters. In [38], the same conclusion was found for single emitter localization and was shown to be independent of the TDOA reference selection when the receivers were *stationary* and *time-synchronized*, with the measurement noise being independent and identically-distributed. These conclusions do not extend to the CIRSLAM framework studied in this paper due to three reasons. The first pertains to the nature of radio SLAM, which is the unknown SOPs' states that are simultaneously estimated along with the navigating vehicles' states. The second arises because the vehicle-mounted receivers' and SOPs' clocks are not necessarily synchronized. The third is because the measurement noise cannot be assumed to be independent and identically-distributed. A preliminary study was conducted in [39], which determined that TOA produces less than or equal estimation error covariance compared to TDOA. However, the analytical findings of the proof were demonstrated using only single run results and details on reducing the communication burden associated with transmitting IMU data as well as the EKF implementation were omitted. In contrast, this paper illustrates the findings of the proof with Monte Carlo runs for different: (i) vehicle-SOP geometries, (ii), SOP clock types, and (iii) SOP measurement qualities. Additionally, this paper provides a complete treatment of the problem, providing necessary details for the interested reader to implement the TOA and TDOA EKF-based CIRSLAM filters.

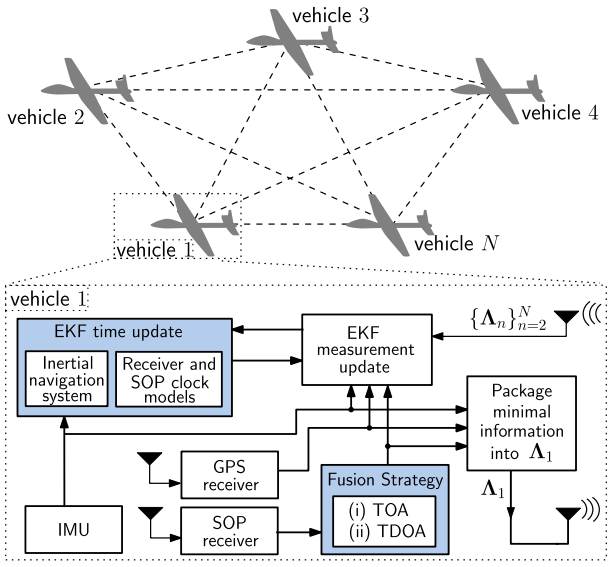

Fig. 1. (a) A High-level diagram of an EKF-based CIRSLAM aided by GNSS (when available) and SOP pseudoranges. The SOP pseudoranges are fused as either: (i) TOA or (ii) TDOA. This fusion takes place by packaging information into $\{\mathbf{\Lambda}_n\}_{n=1}^N$ and broadcasting them.

To reduce the communication burden associated with transmitting IMU data, vehicles can transmit state estimates and associated covariances. To deal with unknown inter-vehicle correlations, covariance intersection fusion has been a popular method of choice [40]–[46]. In contrast to prior approaches, this paper maintains inter-vehicle correlations and deals with the communication burden by determining the minimal sufficient INS information that must be communicated to maintain consistent estimates. The derived sufficient information is discussed and the reduction in communicated data is characterized.

III. Problem Description

A high-level block diagram of the developed CIRSLAM framework that enables a team of N navigating vehicles to share INS data, GNSS pseudoranges, and SOP observables is illustrated in Fig. 1(a). During the time between measurement epochs, each of the n vehicles, where $n = 1, \ldots, N$, uses its IMU data and clock model to perform an EKF time update and then packages INS information into $\mathbf{\Lambda}_n$ to share it with the other navigating vehicles. At each measurement epoch, receivers equipped on each vehicle produce pseudoranges to GNSS satellites (when GNSS signals are available) and observables to SOP emitters. This information is then combined with all $\{\mathbf{\Lambda}_n\}_{n=1}^N$ and is sent to a local EKF measurement update step to perform a tightly-coupled fusion. This paper answers two questions regarding how the INS, GNSS, and SOP information should be shared between the navigating vehicles and fused in their navigation filters: 1) how should SOP observables be fused: (i) TOA or (ii) TDOA? 2) What INS information should be packaged into $\mathbf{\Lambda}_n$ and communicated, so that consistent vehicle position estimates are produced while maintaining minimal communicated data?

IV. Model Description

In this section, the dynamics model of the SOP transmitters and the vehicles' states as well as the measurement models are provided. These models are used in the subsequent sections for the development of the EKF-based CIRSLAM framework.

A. SOP Dynamics Model

Each SOP will be assumed to emanate from a spatially-stationary terrestrial transmitter, and its state vector will consist of its three-dimensional (3-D) position states $\boldsymbol{r}_{\text{sop},m} \triangleq \left[x_{\text{sop},m},\, y_{\text{sop},m},\, z_{\text{sop},m}\right]^{\mathsf{T}} \in \mathbb{R}^3$ and clock error states $\boldsymbol{x}_{\text{clk,sop},m} \triangleq [c\delta t_{\text{sop},m},\, c\dot{\delta} t_{\text{sop},m}]^{\mathsf{T}} \in \mathbb{R}^2$, where c is the speed of light, $\delta t_{\text{sop},m}$ is the clock bias, $\dot{\delta} t_{\text{sop},m}$ is the clock drift, $m = 1, \ldots, M$, and M is the total number of SOPs.

The SOP's discretized dynamics are given by

$$\boldsymbol{x}_{\text{sop},m}(k+1) = \mathbf{F}_{\text{sop}}\, \boldsymbol{x}_{\text{sop},m}(k) + \boldsymbol{w}_{\text{sop},m}(k), \quad k = 1, 2, \ldots,$$
$$\mathbf{F}_{\text{sop}} = \begin{bmatrix} \mathbf{I}_{3\times 3} & \mathbf{0}_{3\times 2} \\ \mathbf{0}_{2\times 3} & \mathbf{F}_{\text{clk}} \end{bmatrix}, \quad \mathbf{F}_{\text{clk}} = \begin{bmatrix} 1 & T \\ 0 & 1 \end{bmatrix}, \tag{1}$$

where $\mathbf{I}_{n\times n}$ denotes the $n \times n$ identity matrix, $\mathbf{0}_{m\times n}$ denotes the $m \times n$ matrix of zeros, T is the constant sampling interval, $\boldsymbol{x}_{\text{sop},m} = \left[\boldsymbol{r}_{\text{sop},m}^{\mathsf{T}},\, \boldsymbol{x}_{\text{clk,sop},m}^{\mathsf{T}}\right]^{\mathsf{T}} \in \mathbb{R}^5$, and $\boldsymbol{w}_{\text{sop},m} \in \mathbb{R}^5$ is the process noise, which is modeled as a discrete-time zero-mean white noise sequence with covariance $\mathbf{Q}_{\text{sop},m} = \text{diag}\left[\mathbf{0}_{3\times 3},\, c^2\mathbf{Q}_{\text{clk,sop},m}\right]$, where

$$\mathbf{Q}_{\text{clk,sop},m} = \begin{bmatrix} S_{w_{\delta t_{\text{sop},m}}} T + S_{w_{\dot{\delta} t_{\text{sop},m}}} \dfrac{T^3}{3} & S_{w_{\dot{\delta} t_{\text{sop},m}}} \dfrac{T^2}{2} \\ S_{w_{\dot{\delta} t_{\text{sop},m}}} \dfrac{T^2}{2} & S_{w_{\dot{\delta} t_{\text{sop},m}}} T \end{bmatrix}.$$

The terms $S_{w_{\delta t_{\text{sop},m}}}$ and $S_{w_{\dot{\delta} t_{\text{sop},m}}}$ are the clock bias and drift process noise power spectra, respectively, which can be related to the power-law coefficients, $\left\{h_{\alpha,\text{sop},m}\right\}_{\alpha=-2}^{2}$, which have been shown through laboratory experiments to characterize the power spectral density of the fractional frequency deviation of an oscillator from nominal frequency according to $S_{\delta t_{\text{sop},m}} \approx \frac{h_{0,\text{sop},m}}{2}$ and $S_{\dot{\delta} t_{\text{sop},m}} \approx 2\pi^2\, h_{-2,\text{sop},m}$ [47].

B. Vehicle Dynamics Model

Let $\{b_n\}$ denote a body frame fixed at the n^{th} navigating vehicle where $n = 1, \ldots, N$ and N is the total number of navigating vehicles, and let $\{g\}$ denote a global frame, e.g., the Earth-centered inertial (ECI) frame [48]. Moreover, let $\boldsymbol{\theta}_{b_n} \in \mathbb{R}^3$ represent the 3-D orientation vector of the body frame with respect to the global frame and $\boldsymbol{r}_{b_n} \in \mathbb{R}^3$ the 3-D position vector of the n^{th} navigating vehicle expressed in $\{g\}$ [49]. Given the n^{th} INS's true 3-D rotational rate vector ${}^{b_n}\boldsymbol{\omega} \in \mathbb{R}^3$ in the body frame and its 3-D acceleration ${}^{g}\boldsymbol{a}_{b_n} \in \mathbb{R}^3$ in the global frame, the standard strapdown kinematics equations can be expressed in continuous time as

$$\dot{\boldsymbol{\theta}}_{b_n}(t) = {}^{b_n}\boldsymbol{\omega}(t), \tag{2}$$
$$\ddot{\boldsymbol{r}}_{b_n}(t) = {}^{g}\boldsymbol{a}_{b_n}(t). \tag{3}$$

In the rest of this paper, the 3-D orientation vector of the body frame with respect to the global frame will be represented by the 4-D quaternion vector ${}^{b_n}_{g}\bar{\boldsymbol{q}} \in \mathbb{R}^4$.

1) IMU Measurement Model: The IMU on the n^{th} navigating vehicle contains a triad-gyroscope and a triad-accelerometer, which produce measurements ${}^{n}\boldsymbol{z}_{\text{imu}} \triangleq \left[{}^{n}\boldsymbol{\omega}_{\text{imu}}^{\mathsf{T}}, {}^{n}\boldsymbol{a}_{\text{imu}}^{\mathsf{T}}\right]^{\mathsf{T}}$ of the angular rate and specific force, which are modeled as

$$ {}^{n}\boldsymbol{\omega}_{\text{imu}}(k) = {}^{b_n}\boldsymbol{\omega}(k) + \boldsymbol{b}_{\text{gyr},n}(k) + \boldsymbol{n}_{\text{gyr},n}(k) \tag{4} $$

$$ {}^{n}\boldsymbol{a}_{\text{imu}}(k) = \mathbf{R}\left[{}^{b_n}_{g}\bar{\boldsymbol{q}}(k)\right]\left({}^{g}\boldsymbol{a}_{b_n}(k) - {}^{g}\boldsymbol{g}_{n}(k)\right) + \boldsymbol{b}_{\text{acc},n}(k) + \boldsymbol{n}_{\text{acc},n}(k), \tag{5} $$

where $\mathbf{R}\left[{}^{b_n}_{g}\bar{\boldsymbol{q}}\right]$ is the equivalent rotation matrix of ${}^{b_n}_{g}\bar{\boldsymbol{q}}$ (see Appendix); ${}^{g}\boldsymbol{g}_{n}$ is the acceleration due to gravity acting on the n^{th} navigating vehicle in the global frame; $\boldsymbol{b}_{\text{gyr},n} \in \mathbb{R}^3$ and $\boldsymbol{b}_{\text{acc},n} \in \mathbb{R}^3$ are the gyroscope and accelerometer biases, respectively; and $\boldsymbol{n}_{\text{gyr},n}$ and $\boldsymbol{n}_{\text{acc},n}$ are measurement noise vectors, which are modeled as zero-mean white noise sequences with covariances $\mathbf{Q}_{\boldsymbol{n}_{\text{gyr},n}}$ and $\mathbf{Q}_{\boldsymbol{n}_{\text{acc},n}}$, respectively.

2) INS State Kinematics: The gyroscope and accelerometer biases in (4)–(5) are dynamic and stochastic; hence, they must be estimated in the EKF as well. As such, the INS 16-state vector is given by

$$ \boldsymbol{x}_{\text{ins},n} = \left[{}^{b_n}_{g}\bar{\boldsymbol{q}}^{\mathsf{T}}, \quad \boldsymbol{r}_{b_n}^{\mathsf{T}}, \quad \dot{\boldsymbol{r}}_{b_n}^{\mathsf{T}}, \quad \boldsymbol{b}_{\text{gyr},n}^{\mathsf{T}}, \quad \boldsymbol{b}_{\text{acc},n}^{\mathsf{T}}\right]^{\mathsf{T}}, $$

where $\dot{\boldsymbol{r}}_{b_n} \in \mathbb{R}^3$ is the 3-D velocity of the navigating vehicle. The INS states evolve in time according to

$$ \boldsymbol{x}_{\text{ins},n}(k+1) = \boldsymbol{f}_{\text{ins}}\left[\boldsymbol{x}_{\text{ins},n}(k), {}^{b_n}\boldsymbol{\omega}(k), {}^{g}\boldsymbol{a}_{b_n}(k)\right], $$

where $\boldsymbol{f}_{\text{ins}}$ is a vector-valued function of standard strapdown kinematic equations, which discretizes (2)–(3) by integrating ${}^{b_n}\boldsymbol{\omega}$ and ${}^{g}\boldsymbol{a}_{b_n}$ to produce ${}^{b_n}_{g}\bar{\boldsymbol{q}}(k+1)$, $\boldsymbol{r}_{b_n}(k+1)$, and $\dot{\boldsymbol{r}}_{b_n}(k+1)$, and uses a velocity random walk model for the biases, which is given by

$$ \boldsymbol{b}_{\text{gyr},n}(k+1) = \boldsymbol{b}_{\text{gyr},n}(k) + \boldsymbol{w}_{\text{gyr},n}(k), \tag{6} $$

$$ \boldsymbol{b}_{\text{acc},n}(k+1) = \boldsymbol{b}_{\text{acc},n}(k) + \boldsymbol{w}_{\text{acc},n}(k), \tag{7} $$

where $\boldsymbol{w}_{\text{gyr},n}$ and $\boldsymbol{w}_{\text{acc},n}$ are process noise vectors that drive the in-run bias variation (or bias instability) and are modeled as white noise sequences with covariance $\mathbf{Q}_{\boldsymbol{w}_{\text{gyr},n}}$ and $\mathbf{Q}_{\boldsymbol{w}_{\text{acc},n}}$, respectively. The INS state vector is augmented with the navigating vehicle-mounted receiver's clock state vector $\boldsymbol{x}_{\text{clk,r},n} \in \mathbb{R}^2$ to obtain the n^{th} navigating vehicle's state vector $\boldsymbol{x}_{\text{r},n} = \left[\boldsymbol{x}_{\text{ins},n}^{\mathsf{T}}, \boldsymbol{x}_{\text{clk,r},n}^{\mathsf{T}}\right]^{\mathsf{T}} \in \mathbb{R}^{18}$.

Remark : While this paper develops an aided INS using an inertial frame (e.g., the ECI frame), other forms of the function $\boldsymbol{f}_{\text{ins}}$ may be used in the CIRSLAM framework, depending on the navigation frame chosen, the mechanization type, and the INS error model used.

3) Receiver Clock State Dynamics: The n^{th} vehicle-mounted receiver's clock states evolve according to

$$ \boldsymbol{x}_{\text{clk,r},n}(k+1) = \mathbf{F}_{\text{clk}}\boldsymbol{x}_{\text{clk,r},n}(k) + \boldsymbol{w}_{\text{clk,r},n}(k), \tag{8} $$

where $\boldsymbol{w}_{\text{clk,r},n} \in \mathbb{R}^2$ is the process noise vector, which is modeled as a discrete-time zero-mean white noise sequence with covariance $\mathbf{Q}_{\text{clk,r},n}$, which has an identical form to $\mathbf{Q}_{\text{clk,sop},m}$, except that $S_{w_{\delta t_{\text{sop},m}}}$ and $S_{w_{\dot{\delta} t_{\text{sop},m}}}$ are now replaced with receiver-specific spectra $S_{w_{\delta t_{\text{r},n}}}$ and $S_{w_{\dot{\delta} t_{\text{r},n}}}$, respectively.

C. Pseudorange Measurement Model

The pseudorange measurements made by the n^{th} receiver on the m^{th} SOP, after discretization and mild approximations discussed in [32], are modeled as

$$ {}^{n}z_{\text{sop},m}(j) = \|\boldsymbol{r}_{b_n}(j) - \boldsymbol{r}_{\text{sop},m}\|_2 + c\cdot\left[\delta t_{\text{r},n}(j) - \delta t_{\text{sop},m}(j)\right] + {}^{n}\upsilon_{\text{sop},m}(j), \tag{9} $$

where ${}^{n}\upsilon_{\text{sop},m}$ is the measurement noise, which is modeled as a discrete-time zero-mean white Gaussian sequence with variance ${}^{n}\sigma^2_{\text{sop},m}$ and $j \in \mathbb{N}$ represents the time index at which $\{{}^{n}z_{\text{sop},m}\}_{n=1}^{N}$ is available, which could be aperiodic. The pseudorange measurement made by the n^{th} receiver on the l^{th} GNSS SV, after compensating for ionospheric and tropospheric delays, is related to the navigating vehicle's states by

$$ {}^{n}z_{\text{sv},l}(j) = \|\boldsymbol{r}_{b_n}(j) - \boldsymbol{r}_{\text{sv},l}(j)\|_2 + c\cdot\left[\delta t_{\text{r},n}(j) - \delta t_{\text{sv},l}(j)\right] + {}^{n}\upsilon_{\text{sv},l}(j), \tag{10} $$

where ${}^{n}z_{\text{sv},l} \triangleq {}^{n}z'_{\text{sv},l} - c\delta t_{\text{iono}} - c\delta t_{\text{tropo}}$; δt_{iono} and δt_{tropo} are the ionospheric and tropospheric delays, respectively; ${}^{n}z'_{\text{sv},l}$ is the uncorrected pseudorange; and ${}^{n}\upsilon_{\text{sv},l}$ is the measurement noise, which is modeled as a discrete-time zero-mean white Gaussian sequence with variance ${}^{n}\sigma^2_{\text{sv},l}$; and $l = 1, \ldots, L$, where L is the total number of GNSS SVs.

V. Collaborative Inertial Radio Simultaneous Localization and Mapping (CIRSLAM)

This section develops the EKF-based CIRSLAM framework, illustrated in Fig. 1, to fuse either TOA or TDOA measurements from unknown SOPs and GNSS pseudoranges (if available) to aid each navigating vehicle's INS using tight coupling. A method to efficiently share INS data between collaborators is also discussed.

A. EKF-Based CIRSLAM Framework

In a CIRSLAM framework, the states of the SOPs are simultaneously estimated along with the states of the navigating vehicles. This can be achieved through an EKF with state vector

$$ \boldsymbol{x} \triangleq \left[\boldsymbol{x}_{\text{r},1}^{\mathsf{T}}, \ldots, \boldsymbol{x}_{\text{r},N}^{\mathsf{T}}, \quad \boldsymbol{x}_{\text{sop},1}^{\mathsf{T}}, \ldots, \boldsymbol{x}_{\text{sop},M}^{\mathsf{T}}\right]^{\mathsf{T}}. $$

The EKF produces an estimate, given by $\hat{\boldsymbol{x}}(k|j) \triangleq \mathbb{E}[\boldsymbol{x}(k)|\boldsymbol{Z}^j]$ of $\boldsymbol{x}(k)$, where $\mathbb{E}[\cdot|\cdot]$ is the conditional expectation operator, $\boldsymbol{Z}^j \triangleq \{\boldsymbol{z}(i)\}_{i=1}^{j}$, $\boldsymbol{z}$ is a vector of INS-aiding measurements (e.g., from GNSS or SOPs), $k \geq j$, and j is the last time-step an INS-aiding measurement was available.

Collaborating navigating vehicles that estimate common states using mutual observations traditionally fuse information (state estimates and/or observations) from each collaborator using one of two main architectures:

- **Centralized:** Each vehicle sends raw sensor data to a central fusion center, which estimates a common state vector and periodically sends the estimate to each vehicle. Centralized architectures produce consistent estimates, i.e., the EKF-produced estimation error covariance

matches the covariance of the actual estimation error, since all inter-vehicle correlations are properly maintained. The drawback is in the large amount of raw sensor data that must be communicated to the central fusion center. Furthermore, the central fusion center is a single point of failure for the system.

- **Distributed:** Each vehicle estimates a copy of the state vector using its own sensor data and then each vehicle shares and fuses these copies using covariance intersection (or one of its variants). Distributed architectures typically require less data transmission between collaborators, since raw sensor data is filtered locally at each vehicle. The drawback is in the difficulty of reaching consensus, i.e., in reaching agreement between the estimate copies, when inter-vehicle correlations are unknown. While covariance intersection techniques are used to fuse estimates with unknown inter-vehicle correlations, they typically produce overly conservative estimates, i.e., the EKF-produced estimation error covariance is larger than the actual covariance of the estimation error.

In contrast to traditional centralized and distributed approaches, the approach of the distributed CIRSLAM framework illustrated in Fig. 1 is for each navigating vehicle to monitor the entire state vector $\boldsymbol{x}$, but to distribute the INSs (the EKF time update step) amongst the navigating vehicles and to optimize what information is shared in $\boldsymbol{\Lambda}_n$ (TOA or TDOA from SOPs and what INS data) and how often $\boldsymbol{\Lambda}_n$ is transmitted for aiding corrections (the EKF update step). This approach eliminates a single point of failure, reduces the amount of transmitted data, and with the appropriate transmitted information in $\boldsymbol{\Lambda}_n$, the entire state vector $\boldsymbol{x}$ that is monitored at any particular vehicle will be brought into consensus with the state vector monitored at all other vehicles. The distributed CIRSLAM framework's operation is summarized in algorithm 1.

Algorithm 1 Distributed CIRSLAM Framework

Given: $\hat{\boldsymbol{x}}(j|j)$ and $\mathbf{P}_{\boldsymbol{x}}(j|j)$, each of the N vehicles conducts the following:

for $n = 1, \ldots, N$

- **Local Prediction:** Locally produce $\hat{\boldsymbol{x}}_{\mathrm{r},n}(k|j)$ using an INS and clock models and $\{\hat{\boldsymbol{x}}_{\mathrm{sop},m}(k|j)\}_{m=1}^{M}$ using SOP dynamics model.
- **Communication:** Package $\hat{\boldsymbol{x}}_{\mathrm{r}_n}(k|j)$, TOA (or TDOA) measurements, and INS data into $\boldsymbol{\Lambda}_n$ and transmit $\boldsymbol{\Lambda}_n$.
- **Assimilation:** Unpack $\{\boldsymbol{\Lambda}_i\}_{i=1}^{N} \backslash n$, assemble $\hat{\boldsymbol{x}}(k|j)$, and produce $\mathbf{P}_{\boldsymbol{x}}(k|j)$.
- **Correction:** Perform EKF measurement update to produce $\hat{\boldsymbol{x}}(k|k)$, and $\mathbf{P}_{\boldsymbol{x}}(k|k)$.

end for

In the following sections, the TOA and TDOA information fusion strategies are developed and compared. Both strategies have a common prediction (time update) step, which uses the on-board INS of each vehicle and clock models. Both strategies use GNSS pseudoranges as TOA measurements if they are available during the correction (measurement update) step. The distinction between these strategies is in how the SOP pseudoranges are fused to aid the navigating vehicles' on-board INSs: either TOA or TDOA with reference to selected SOPs.

B. Local Prediction

Each vehicle only locally produces a prediction of its own state vector $\hat{\boldsymbol{x}}_{\mathrm{r},n}(k|j)$ and of the SOPs' $\{\hat{\boldsymbol{x}}_{\mathrm{sop},m}(k|j)\}_{m=1}^{M}$. The full state prediction $\hat{\boldsymbol{x}}(k|j)$ and the corresponding prediction error covariance $\mathbf{P}_{\boldsymbol{x}}(k|j)$ become available locally during the assimilation step, which is described in Subsection V-D.

1) State Prediction: To produce $\hat{\boldsymbol{x}}_{\mathrm{r},n}(k|j) = \left[\hat{\boldsymbol{x}}_{\mathrm{ins},n}^{\mathsf{T}}(k|j), \hat{\boldsymbol{x}}_{\mathrm{clk,r},n}^{\mathsf{T}}(k|j)\right]^{\mathsf{T}}$, the INS on-board the n^{th} navigating vehicle integrates ${}^{n}\boldsymbol{z}_{\mathrm{imu}}$ between aiding updates to produce a prediction of $\boldsymbol{x}_{\mathrm{ins},n}$. The one-step prediction is given by

$$\hat{\boldsymbol{x}}_{\mathrm{ins},n}(j+1|j) = \boldsymbol{f}_{\mathrm{ins}}\left[\hat{\boldsymbol{x}}_{\mathrm{ins},n}(j|j), {}^{b_n}\hat{\boldsymbol{\omega}}(j), {}^{g}\hat{\boldsymbol{a}}_{b_n}(j)\right], \quad (11)$$

where ${}^{b_n}\hat{\boldsymbol{\omega}}(j)$ and ${}^{g}\hat{\boldsymbol{a}}_{b_n}(j)$ are the estimates of ${}^{b_n}\boldsymbol{\omega}(j)$ and ${}^{g}\boldsymbol{a}_{b_n}(j)$, respectively, obtained from (4)–(5) and $\hat{\boldsymbol{x}}_{\mathrm{ins},n}(j|j)$ [30], and the function $\boldsymbol{f}_{\mathrm{ins}}$ contains standard INS equations, which are described in [50], [51]. Assuming there are κ time-steps between aiding updates, the navigating vehicle uses IMU data $\{{}^{n}\boldsymbol{z}_{\mathrm{imu}}(i)\}_{i=j}^{k}$ to recursively solve (11) to produce $\hat{\boldsymbol{x}}_{\mathrm{ins}_n}(k|j)$, where $k \equiv j + \kappa$. The vehicle-mounted receiver's κ-step clock state prediction follows from (8) and is given by

$$\hat{\boldsymbol{x}}_{\mathrm{clk,r},n}(k|j) = \mathbf{F}_{\mathrm{clk}}^{\kappa}\hat{\boldsymbol{x}}_{\mathrm{clk,r},n}(j|j),$$

where

$$\mathbf{F}_{\mathrm{clk}}^{\kappa} \triangleq \begin{cases} \mathbf{I}_{2\times 2} & \kappa = 0 \\ \prod_{i=1}^{\kappa}\mathbf{F}_{\mathrm{clk}} & \kappa > 0, \end{cases}$$

The SOPs' κ-step state prediction, which follows from (1), is given by

$$\hat{\boldsymbol{x}}_{\mathrm{sop},m}(k|j) = \mathbf{F}_{\mathrm{sop}}^{\kappa}\hat{\boldsymbol{x}}_{\mathrm{sop},m}(j|j), \quad m = 1, \ldots, M.$$

2) Prediction Error Covariance: Although the prediction error covariance is not produced at this point in the algorithm, its computation is presented here to explain why it cannot be produced until assimilation, which is discussed in Subsection V-D. The κ-step covariance prediction is given by

$$\begin{aligned} \mathbf{P}_{\boldsymbol{x}}(k|j) &= \mathbf{F}(k,j)\mathbf{P}_{\boldsymbol{x}}(j|j)\mathbf{F}^{\mathsf{T}}(k,j) + \mathbf{Q}^{+}(k,j), \quad (12) \\ \mathbf{F}(k,j) &\triangleq \mathrm{diag}\left[\mathbf{F}_{\mathrm{r},1}(k,j), \ldots, \mathbf{F}_{\mathrm{r},N}(k,j), \right. \\ &\qquad \left. \mathbf{F}_{\mathrm{sop}}^{\kappa}, \ldots, \mathbf{F}_{\mathrm{sop}}^{\kappa}\right], \\ \mathbf{F}_{\mathrm{r},n}(k,j) &\triangleq \mathrm{diag}\left[\Phi_{\mathrm{ins},n}(k,j), \mathbf{F}_{\mathrm{clk}}^{\kappa}\right], \\ \Phi_{\mathrm{ins},n}(k,j) &\triangleq \prod_{i=j}^{k}\Phi_{\mathrm{ins},n}(i), \quad (13) \end{aligned}$$

where $\Phi_{\mathrm{ins},n}(i)$ is the Jacobian of $\boldsymbol{f}_{\mathrm{ins}}$ evaluated at $\hat{\boldsymbol{x}}_{\mathrm{ins},n}(i|j)$. The structure of $\Phi_{\mathrm{ins},n}(i)$ is provided in Appendix. The matrix

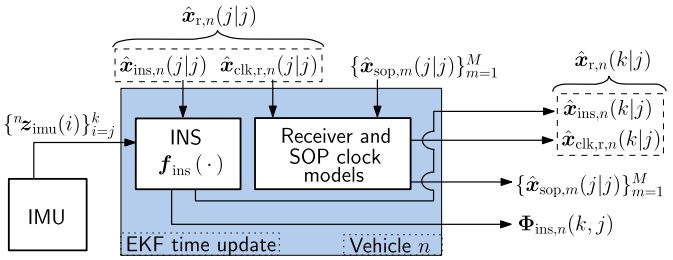

Fig. 2. Local prediction for vehicle n. The inputs are IMU data $\{{}^{n}\boldsymbol{z}_{\mathrm{imu}}(i)\}_{i=j}^{k}$ and the current state estimates $\hat{\boldsymbol{x}}_{\mathrm{r},n}(j|j)$ and $\{\hat{\boldsymbol{x}}_{\mathrm{sop},m}(j|j)\}_{m=1}^{M}$. The outputs are the time updates $\hat{\boldsymbol{x}}_{\mathrm{r},n}(k|j)$ and $\{\hat{\boldsymbol{x}}_{\mathrm{sop},m}(k|j)\}_{m=1}^{M}$ and the Jacobian $\Phi_{\mathrm{ins},n}(k,j)$.

$\mathbf{Q}^{+}(k,j)$ is the propagated process noise covariance, which has the form

$$\begin{aligned}\mathbf{Q}^{+}(k,j) \triangleq \operatorname{diag}\big[&\mathbf{Q}^{+}_{\mathrm{r},1}(k,j),\ldots,\mathbf{Q}^{+}_{\mathrm{r},N}(k,j),\\ &\mathbf{Q}^{+}_{\mathrm{sop},1}(k,j),\ \ldots,\ \mathbf{Q}^{+}_{\mathrm{sop},M}(k,j)\big],\\ \mathbf{Q}^{+}_{\mathrm{r},n}(k,j) \triangleq \sum_{i=j}^{k}&\mathbf{F}_{\mathrm{r},n}(i,j)\mathbf{Q}_{\mathrm{r},n}(i)\mathbf{F}^{\mathsf{T}}_{\mathrm{r},n}(i,j),\\ \mathbf{Q}^{+}_{\mathrm{sop},m}(k,j) \triangleq \sum_{i=j}^{k}&\mathbf{F}^{(i-j)}_{\mathrm{sop}}\mathbf{Q}_{\mathrm{sop},m}[\mathbf{F}^{\mathsf{T}}_{\mathrm{sop}}]^{(i-j)},\end{aligned}$$

where $\mathbf{Q}_{\mathrm{r},n}(i) \triangleq \operatorname{diag}\left[\mathbf{Q}_{\mathrm{ins},n}(i),\ c^2\mathbf{Q}_{\mathrm{clk,r},n}\right]$ and $\mathbf{Q}_{\mathrm{ins},n}$ is the n^{th} navigating vehicle's discrete-time linearized INS process noise covariance. The structure of $\mathbf{Q}_{\mathrm{ins},n}(i)$ is provided in Appendix. The local prediction for vehicle n is illustrated in Fig. 2.

Note that at this point in the algorithm, the prediction error covariance (12) cannot be computed at vehicle n, $\forall\, n \in \{1,\ldots,N\}$, since all matrices $\{\Phi_{\mathrm{ins},n}(k,j)\}_{n=1}^{N}$ are not available at each vehicle. In the next subsection, it is shown what INS information each vehicle transmits, so that (12) may be computed at each vehicle during the assimilation step.

C. Vehicle-to-Vehicle Communication

To produce the prediction error covariance (12) at each vehicle, the matrices $\{\Phi_{\mathrm{ins},n}(k,j)\}_{n=1}^{N}$ must be available. It can been seen in Appendix that the components of these matrices are a function of IMU data from each respective navigating vehicle. Therefore, two possible approaches to make $\{\Phi_{\mathrm{ins},n}(k,j)\}_{n=1}^{N}$ available to each vehicle are: 1) each vehicle communicates its raw IMU data or 2) each vehicle communicates the full matrix (13). On one hand, IMU data rates are typically between 100 Hz to 400 Hz, with 6 floating-point values per data sample. On the other hand, the matrix (13) is in $\mathbb{R}^{15\times 15}$, requiring the transmission of 225 floating-point values every EKF measurement update, which typically takes place between 5 Hz to 10 Hz. These data rates make the transmission of either raw accelerometer and gyroscope data or the matrix (13) undesirable for several reasons: (i) large communication bandwidth, (ii) packet drops due to lossy communication channels, and (iii) privacy concerns. Consider an application nearby an airport or takeoff/landing facility with dozens of UAVs. Communicating data unnecessarily when the number of communicators scales up would consume the spectrum, which is a very scarce resource.

To address this communication burden, instead of transmitting raw IMU data or the full matrix (13), a packet $\Lambda_{\mathrm{ins},n}$ containing minimal sufficient INS information to reconstruct an approximation of (13) with minimal degradation in performance is transmitted once per κ-step propagation. To derive the sufficient INS information to be communicated, the structure of (13) after a κ-step propagation is investigated. After carrying out κ successive multiplications, the form of matrix (13) becomes approximately

$$\begin{aligned}&\boldsymbol{\Phi}_{\mathrm{ins},n}(k,j)\\ &\approx\begin{bmatrix}\mathbf{I}_{3\times3} & \mathbf{0}_{3\times3} & \mathbf{0}_{3\times3} & \kappa T\mathbf{R}[\bar{\boldsymbol{q}}_{1,n}] & \mathbf{0}_{3\times3}\\ \lfloor \boldsymbol{v}_{1,n}\times\rfloor & \mathbf{I}_{3\times3} & \mathbf{I}_{3\times3}T & \boldsymbol{\Phi}_{1,n} & \frac{\kappa T^2}{2}\mathbf{R}[\bar{\boldsymbol{q}}_{2,n}]\\ \lfloor \boldsymbol{v}_{2,n}\times\rfloor & \mathbf{0}_{3\times3} & \mathbf{I}_{3\times3} & \boldsymbol{\Phi}_{2,n} & \kappa T\mathbf{R}[\bar{\boldsymbol{q}}_{1,n}]\\ \mathbf{0}_{3\times3} & \mathbf{0}_{3\times3} & \mathbf{0}_{3\times3} & \mathbf{I}_{3\times3} & \mathbf{0}_{3\times3}\\ \mathbf{0}_{3\times3} & \mathbf{0}_{3\times3} & \mathbf{0}_{3\times3} & \mathbf{0}_{3\times3} & \mathbf{I}_{3\times3}\end{bmatrix},\end{aligned} \tag{14}$$

where $\kappa = k-j$; $\lfloor \boldsymbol{v}_{1,n}\times\rfloor \in \mathbb{R}^{3\times3}$ and $\lfloor \boldsymbol{v}_{2,n}\times\rfloor \in \mathbb{R}^{3\times3}$ are skew symmetric matrices whose elements are defined from the vectors $\boldsymbol{v}_{1,n} \in \mathbb{R}^3$ and $\boldsymbol{v}_{2,n} \in \mathbb{R}^3$, respectively; the matrices $\mathbf{R}[\bar{\boldsymbol{q}}_{1,n}] \in \mathbb{R}^{3\times3}$ and $\mathbf{R}[\bar{\boldsymbol{q}}_{2,n}] \in \mathbb{R}^{3\times3}$ are rotation matrices; and $\boldsymbol{\Phi}_{1,n} \in \mathbb{R}^{3\times3}$ and $\boldsymbol{\Phi}_{2,n} \in \mathbb{R}^{3\times3}$ are arbitrarily structured matrices.

Note the following two properties of the structure (14). First, since $\lfloor \boldsymbol{v}_{1,n}\times\rfloor$ and $\lfloor \boldsymbol{v}_{2,n}\times\rfloor$ maintain a skew symmetric form, they can be transmitted using only three elements each. Second, the scaling pre-multiplying the matrices $\mathbf{R}[\bar{\boldsymbol{q}}_{1,n}]$ and $\mathbf{R}[\bar{\boldsymbol{q}}_{2,n}]$ is deterministic and only dependent on the IMU sampling period T and the number of iterations κ; therefore, these matrices can be converted to quaternions $\bar{\boldsymbol{q}}_{1,n}$ and $\bar{\boldsymbol{q}}_{2,n}$ and then transmitted using only four elements each. From these properties, the sufficient INS information to package for transmission is found to be

$$\boldsymbol{\Lambda}_{\mathrm{ins},n} \triangleq \left\{\boldsymbol{v}_{1,n}, \boldsymbol{v}_{2,n}, \bar{\boldsymbol{q}}_{1,n}, \bar{\boldsymbol{q}}_{2,n}, \boldsymbol{\Phi}_{1,n}, \boldsymbol{\Phi}_{2,n}\right\},$$

which only requires the transmission of 32 floating-point values every EKF measurement update. When EKF updates happen at the rate of SOP measurements T_{sop}, transmitting $\boldsymbol{\Lambda}_{\mathrm{ins},n}$ instead of IMU data or the matrix (13) reduces the number of transmitted floating-point values by at least

$$\left[1 - \frac{32}{\min\left\{6\times\frac{T_{\mathrm{sop}}}{T_{\mathrm{imu}}}, 225\right\}}\right]\times 100\%,$$

where $\min\{a,b\}$ returns the smallest value among a and b. The tradeoff for significantly reducing the amount of communicated data is in positioning performance. Specifically, the vehicles' position estimation errors increase due to the approximation in (14), which arises due to the rotation matrices $\mathbf{R}[\bar{\boldsymbol{q}}_{1,n}]$ and $\mathbf{R}[\bar{\boldsymbol{q}}_{2,n}]$ deviating from true rotation matrices as T_{sop} increases. The increase in position error was shown to be minimal for typical values of T_{sop} and moderate probability of packet loss [52].

The INS information $\Lambda_{\text{ins},n}$ is packaged inside of $\mathbf{\Lambda}_n$, along with other necessary information for each vehicle to produce an EKF update, and then is broadcasted by the n^{th} vehicle at the fixed rate of measurement epochs. The packet $\mathbf{\Lambda}_n$ is given by

$$\mathbf{\Lambda}_n(k) \triangleq \left\{\hat{\boldsymbol{x}}_{\text{ins},n}(k|j), \mathbf{\Lambda}_{\text{ins},n}(k, j), {}^n\boldsymbol{z}_{\text{sv}}(k), {}^n\boldsymbol{z}_{\text{sop}}(k)\right\}, \quad (15)$$

where ${}^n\boldsymbol{z}_{\text{sv}}$ and ${}^n\boldsymbol{z}_{\text{sop}}$ are GNSS and SOP pseudoranges, respectively, which are discussed further for each strategy in the following subsections.

In practice, the sharing of these packets over a wireless channel may cause their contents to be corrupted with errors. If the errors can be detected, the corrupted packets may be discarded. When the packets $\mathbf{\Lambda}_n$ are transmitted at 5Hz, which is the sharing rate used in this paper, around only 1 meter of error is introduced when 60% of the packets were discarded [52].

D. Assimilation

Assuming a fully-connected graph, as in Fig. 1, the packets $\{\mathbf{\Lambda}_n(k)\}_{n=1}^N$ contain all components of the state prediction to computer $\hat{\boldsymbol{x}}(k|j)$ and (12). To compute (12), the matrix $\mathbf{F}(k, j)$ is first assembled by using the information in $\{\mathbf{\Lambda}_{\text{ins},n}\}_{n=1}^N$. The vectors $\boldsymbol{v}_{1,n}$ and $\boldsymbol{v}_{2,n}$ are used to reconstruct the skew-symmetric matrices $\lfloor \boldsymbol{v}_{1,n}\times\rfloor$ and $\lfloor \boldsymbol{v}_{2,n}\times\rfloor$ in (14) through

$$\lfloor \boldsymbol{a}\times\rfloor = \begin{bmatrix} 0 & -a_3 & a_2 \\ a_3 & 0 & -a_1 \\ -a_2 & a_1 & 0 \end{bmatrix}, \quad \boldsymbol{a} \triangleq \begin{bmatrix} a_1 \\ a_2 \\ a_3 \end{bmatrix}. \quad (16)$$

The quaternions $\bar{\boldsymbol{q}}_{1,n}$ and $\bar{\boldsymbol{q}}_{2,n}$ are converted to rotation matrices through

$$\mathbf{R}[\bar{\boldsymbol{q}}] = \mathbf{I}_{3\times 3} - q_4\lfloor \boldsymbol{q}\times\rfloor + 2\lfloor \boldsymbol{q}\times\rfloor^2,$$

where $\bar{\boldsymbol{q}} \triangleq [\boldsymbol{q}, q_0]^{\mathsf{T}} = [q_1, q_2, q_3, q_0]^{\mathsf{T}}$ and q_0 is the real component of the quaternion. Each vehicle may now compute the EKF measurement update and the corresponding corrected estimation error covariance. In the following two subsections, the correction equations are developed for two information fusion strategies: (1) TOA and (2) TDOA with SOP referencing.

E. TOA Information Fusion Strategy

In this subsection, the EKF-based CIRSLAM measurement update for fusing TOA measurements from SOPs is described. Specifically, the correction to the estimation error $\tilde{\boldsymbol{x}}(k|k)$ is provided, since it will be compared with the estimation error of the TDOA fusion strategy, denoted $\tilde{\tilde{\boldsymbol{x}}}(k|k)$, in Section VI.

1) TOA Measurements: The EKF measurement update will correct the navigating vehicles' INS and clock errors given the measurement vector

$$\begin{aligned} \boldsymbol{z} &\triangleq \left[\boldsymbol{z}_{\text{sv}}^{\mathsf{T}}, \boldsymbol{z}_{\text{sop}}^{\mathsf{T}}\right]^{\mathsf{T}}, \\ \boldsymbol{z}_{\text{sv}} &\triangleq \left[{}^1\boldsymbol{z}_{\text{sv}}^{\mathsf{T}}, \ldots, {}^N\boldsymbol{z}_{\text{sv}}^{\mathsf{T}}\right]^{\mathsf{T}}, \quad \boldsymbol{z}_{\text{sop}} \triangleq \left[{}^1\boldsymbol{z}_{\text{sop}}^{\mathsf{T}}, \ldots, {}^N\boldsymbol{z}_{\text{sop}}^{\mathsf{T}}\right]^{\mathsf{T}}, \\ {}^n\boldsymbol{z}_{\text{sv}} &= \left[{}^n z_{\text{sv},1}, \ldots, {}^n z_{\text{sv},L}\right]^{\mathsf{T}}, {}^n\boldsymbol{z}_{\text{sop}} = \left[{}^n z_{\text{sop},1}, \ldots, {}^n z_{\text{sop},M}\right]^{\mathsf{T}}. \end{aligned} \quad (17)$$

The correction equations are described next for: GNSS availability ($L > 0$) and GNSS unavailability ($L = 0$).

2) TOA Correction Equations: Given a prediction error $\tilde{\boldsymbol{x}}(k|j)$, the error correction and corresponding corrected error covariance are given by

$$\begin{aligned} \tilde{\boldsymbol{x}}(k|k) &= \tilde{\boldsymbol{x}}(k|j) - \mathbf{L}(k)\mathbf{S}^{-1}(k)\boldsymbol{v}(k), \\ \mathbf{P}_{\boldsymbol{x}}(k|k) &= \mathbf{P}_{\boldsymbol{x}}(k|j) - \mathbf{L}(k)\mathbf{S}^{-1}(k)\mathbf{L}^{\mathsf{T}}(k), \quad (18) \\ \mathbf{L}(k) &\triangleq \mathbf{P}_{\boldsymbol{x}}(k|j)\mathbf{H}^{\mathsf{T}}(k), \quad (19) \\ \mathbf{S}(k) &\triangleq \mathbf{H}(k)\mathbf{L}(k) + \mathbf{R}(k), \quad (20) \\ \boldsymbol{v}(k) &\triangleq \boldsymbol{z}(k) - \hat{\boldsymbol{z}}(k|j), \quad (21) \end{aligned}$$

where $\hat{\boldsymbol{z}}(k|j)$ is a vector containing the predicted GNSS pseudoranges and the predicted SOP TOA measurement set. The matrix $\mathbf{H}$ is the measurement Jacobian and has the form

$$\begin{aligned} \mathbf{H} &= \begin{bmatrix} \mathbf{H}_{\text{sv,r}} & \mathbf{0}_{NL\times 5M} \\ \mathbf{H}_{\text{sop,r}} & \mathbf{H}_{\text{sop}} \end{bmatrix}, \\ \mathbf{H}_{\text{sv,r}} &\triangleq \text{diag}\left[{}^1\mathbf{H}_{\text{sv,r}}, \ldots, {}^N\mathbf{H}_{\text{sv,r}}\right], \\ {}^n\mathbf{H}_{\text{sv},r} &= \begin{bmatrix} \mathbf{0}_{1\times 3} & {}^n\hat{\mathbf{1}}_{\text{sv},1}^{\mathsf{T}} & \mathbf{0}_{1\times 9} & \boldsymbol{h}_{\text{clk}}^{\mathsf{T}} \\ \vdots & \vdots & \vdots & \vdots \\ \mathbf{0}_{1\times 3} & {}^n\hat{\mathbf{1}}_{\text{sv},L}^{\mathsf{T}} & \mathbf{0}_{1\times 9} & \boldsymbol{h}_{\text{clk}}^{\mathsf{T}} \end{bmatrix}, \\ \mathbf{H}_{\text{sop,r}} &\triangleq \text{diag}\left[{}^1\mathbf{H}_{\text{sop,r}}, \ldots, {}^N\mathbf{H}_{\text{sop,r}}\right], \end{aligned}$$

where ${}^n\mathbf{H}_{\text{sop,r}}$ has the same structure as ${}^n\mathbf{H}_{\text{sv,r}}$, except ${}^n\hat{\mathbf{1}}_{\text{sv},l}^{\mathsf{T}}$ is replaced with ${}^n\hat{\mathbf{1}}_{\text{sop},m}^{\mathsf{T}}$,

$$\begin{aligned} \mathbf{H}_{\text{sop}} &\triangleq \left[{}^1\mathbf{H}_{\text{sop}}^{\mathsf{T}}, \ldots, {}^N\mathbf{H}_{\text{sop}}^{\mathsf{T}}\right]^{\mathsf{T}}, \\ {}^n\mathbf{H}_{\text{sop}} &= \text{diag}\left[{}^n\mathbf{H}_{\text{sop},1}, \ldots, {}^n\mathbf{H}_{\text{sop},M}\right], \\ {}^n\hat{\mathbf{1}}_{\text{sv},l} &\triangleq \frac{\hat{\boldsymbol{r}}_{b_n} - \boldsymbol{r}_{\text{sv},l}}{\|\hat{\boldsymbol{r}}_{b_n} - \boldsymbol{r}_{\text{sv},l}\|}, \quad {}^n\hat{\mathbf{1}}_{\text{sop},m} \triangleq \frac{\hat{\boldsymbol{r}}_{b_n} - \hat{\boldsymbol{r}}_{\text{sop},m}}{\|\hat{\boldsymbol{r}}_{b_n} - \hat{\boldsymbol{r}}_{\text{sop},m}\|}, \\ {}^n\mathbf{H}_{\text{sop},m} &\triangleq \left[-{}^n\hat{\mathbf{1}}_{\text{sop},m}^{\mathsf{T}}, -\boldsymbol{h}_{\text{clk}}^{\mathsf{T}}\right], \quad \boldsymbol{h}_{\text{clk}} \triangleq [1, 0]^{\mathsf{T}}, \end{aligned}$$

and $\mathbf{R}$ is the measurement noise covariance. Note that $\mathbf{R}$ is not necessarily diagonal, since there are no assumptions made on the measurement noise statistics, except that $\mathbf{R} \succ \mathbf{0}$.

Note that if GNSS pseudoranges become completely unavailable, i.e., $L = 0$ and $\boldsymbol{z} \equiv \boldsymbol{z}_{\text{sop}}$, the state and covariance corrections are identical, except that the Jacobian is adjusted to account for GNSS SV pseudoranges no longer being available, specifically

$$\mathbf{H} \equiv \left[\mathbf{H}_{\text{sop},r}, \mathbf{H}_{\text{sop}}\right]. \quad (22)$$

F. TDOA With SOP Referencing Information Fusion Strategy

In this information fusion strategy, TDOA measurements are computed at each vehicle-mounted receiver by differencing the drawn pseudoranges with a selected reference SOP. The produced estimation error and corresponding covariance of $\boldsymbol{x}$ when TDOA measurements are used will be denoted $\tilde{\tilde{\boldsymbol{x}}}$, and $\mathbf{P}_{\tilde{\boldsymbol{x}}}$, respectively.

1) TDOA Measurements: Each navigating vehicle is free to select an arbitrary reference SOP, i.e., the SOP measurement set computed by the n^{th} navigating vehicle becomes

$$\begin{aligned} {}^{n}\bar{\boldsymbol{z}}_{\text{sop}}^{\mathsf{T}} &\triangleq \left[{}^{n}\bar{z}_{\text{sop},1}, \ldots, {}^{n}\bar{z}_{\text{sop},M}\right]^{\mathsf{T}}, \\ {}^{n}\bar{z}_{\text{sop},m} &\triangleq {}^{n}z_{\text{sop},m} - {}^{n}z_{\text{sop},\iota_n} \\ &= \|\boldsymbol{r}_{b_n}(j) - \boldsymbol{r}_{\text{sop},m}\|_2 - \|\boldsymbol{r}_{b_n}(j) - \boldsymbol{r}_{\text{sop},\iota_n}\|_2 \\ &\quad + c \cdot [\delta t_{\text{sop},m}(j) - \delta t_{\text{sop},\iota_n}(j)] \\ &\quad + {}^{n}v_{\text{sop},m}(j) - {}^{n}v_{\text{sop},\iota_n}(j), \end{aligned} \tag{23}$$

where ι_n is the reference SOP number used by the n^{th} vehicle and $m \in \{1, \ldots, M\} \backslash \iota_n$. Each vehicle replaces the SOP TOA measurements z_{sop} with the SOP TDOA measurements $\bar{z}_{\text{sop}}$ in the transmitted packet (15). Note that since the SOP transmitters are *not synchronized*, the TDOA measurements (23) are parameterized by the clock biases of both transmitters; therefore, both of these biases must be estimated. This differs from traditional TDOA-based localization approaches that assume synchronized transmitters, which allow for these biases to cancel and to be removed from the estimator.

The measurement set available to each vehicle-mounted receiver in the TDOA fusion strategy may be written in terms of the measurement set (17) of the TOA fusion strategy as

$$\bar{z} \triangleq \begin{bmatrix} z_{\text{sv}} \\ \bar{z}_{\text{sop}} \end{bmatrix} = \begin{bmatrix} \mathbf{I}_{NL\times NL} & \mathbf{0}_{NL\times NM} \\ \mathbf{0}_{NM\times NL} & \mathbf{T} \end{bmatrix} \begin{bmatrix} z_{\text{sv}} \\ z_{\text{sop}} \end{bmatrix} \triangleq \Xi z, \tag{24}$$

where $\mathbf{T}$ is the difference operator matrix that maps z_{sop} to $\bar{z}_{\text{sop}}$, which has the form

$$\mathbf{T} = \text{diag}\left[\mathbf{T}_{\iota_1}, \ldots \mathbf{T}_{\iota_N}\right], \tag{25}$$

$$\mathbf{T}_{\iota_n} = \begin{bmatrix} 1 & \ldots & 0 & -1 & 0 & \ldots & 0 \\ \vdots & \ddots & \vdots & \vdots & \vdots & \ddots & \vdots \\ 0 & \ldots & 1 & -1 & 0 & \ldots & 0 \\ 0 & \ldots & 0 & -1 & 1 & \ldots & 0 \\ \vdots & \ddots & \vdots & \vdots & \vdots & \ddots & \vdots \\ 0 & \ldots & 0 & -1 & 0 & \ldots & 1 \end{bmatrix}, \tag{26}$$

where the column of "−1" resides in column ι_n. The structure of the prediction error covariance $\mathbf{P}_{\tilde{x}}(k|j)$ is not dependent on the fusion strategy; therefore, it has the same form as (12). The correction equations are summarized next.

2) TDOA Correction Equations: Given a prediction error $\tilde{\tilde{\boldsymbol{x}}}(k|j)$, the error correction and corresponding corrected error covariance are given by:

$$\tilde{\tilde{\boldsymbol{x}}}(k|k) = \tilde{\tilde{\boldsymbol{x}}}(k|j) - \bar{\mathbf{L}}(k)\bar{\mathbf{S}}^{-1}\bar{\boldsymbol{\nu}}(k), \tag{27}$$

$$\mathbf{P}_{\tilde{x}}(k|k) = \mathbf{P}_{\tilde{x}}(k|j) - \bar{\mathbf{L}}(k)\bar{\mathbf{S}}^{-1}(k)\bar{\mathbf{L}}^{\mathsf{T}}(k), \tag{28}$$

$$\bar{\mathbf{L}}(k) \triangleq \mathbf{P}_{\tilde{x}}(k|j)\bar{\mathbf{H}}^{\mathsf{T}}(k) \tag{29}$$

$$\bar{\mathbf{S}}(k) \triangleq \bar{\mathbf{H}}(k)\bar{\mathbf{L}}(k) + \bar{\mathbf{R}}(k) \tag{30}$$

$$\bar{\boldsymbol{\nu}}(k) \triangleq \bar{z}(k) - \hat{\bar{z}}(k|j), \tag{31}$$

where $\hat{\bar{z}}(k|j)$ is the predicted GNSS pseudoranges and SOP TDOA measurement set and $\bar{\mathbf{H}}$ is the corresponding measurement Jacobian, which is related to $\mathbf{H}$ through

$$\bar{\mathbf{H}} \triangleq \begin{bmatrix} \mathbf{I}_{NL\times NL} & \mathbf{0}_{NL\times NM} \\ \mathbf{0}_{NM\times NL} & \mathbf{T} \end{bmatrix} \begin{bmatrix} \mathbf{H}_{\text{sv},r} & \mathbf{0}_{NL\times 5M} \\ \mathbf{H}_{\text{sop},r} & \mathbf{H}_{\text{sop}} \end{bmatrix}.$$

The measurement noise covariance is given by $\bar{\mathbf{R}} = \Xi\mathbf{R}\Xi^{\mathsf{T}}$.

Note that if GNSS pseudoranges become completely unavailable ($L = 0$), i.e., $\bar{z} \equiv \bar{z}_{\text{sop}}$, the state and covariance corrections are identical to when $L > 0$, except that the dimension of $\mathbf{I}_{NL\times NL}$ reduces to zero, modifying the measurement Jacobian to take the form

$$\bar{\mathbf{H}} = \mathbf{T}\mathbf{H}, \tag{32}$$

where $\mathbf{H}$ is the measurement Jacobian (22) from the TOA fusion strategy when $L = 0$.

VI. Information Fusion Strategy Performance Comparison

This section studies the estimation performance of the two information fusion strategies presented in Section V. First, it is shown that the TDOA estimation performance is invariant to the SOP reference selection. Then, it is shown that the TOA strategy yields less than or equal (in a positive semi-definite sense) estimation error covariance corresponding to the navigating vehicles' positions than the TDOA strategy.

A. TDOA SOP Reference Selection

In this subsection, it is shown that the estimation error and error covariance are invariant to the choice of the SOP reference, as summarized in Theorem 1.

Theorem 1: Consider an environment comprising N receivers and M unknown SOPs with arbitrary: (i) receiver and SOP clock qualities (i.e., arbitrary $\{\mathbf{Q}_{\text{clk,r},n}\}_{n=1}^{N}$ and $\{\mathbf{Q}_{\text{clk,sop},m}\}_{m=1}^{M}$), (ii) geometric configurations, and (iii) measurement noise covariance (i.e., $\mathbf{R} \succ \mathbf{0}$, but not necessarily diagonal). The EKF-based CIRSLAM yields an estimation error and corresponding estimation error covariance that are invariant to each receiver's SOP reference selection.

Proof: The proof will only consider GNSS unavailability periods ($L = 0$), i.e., $\bar{z} \equiv \bar{z}_{\text{sop}}$. The proof can be straightforwardly extended to GNSS availability ($L > 0$). Given $\tilde{\tilde{\boldsymbol{x}}}(k|j)$, the correction $\tilde{\tilde{\boldsymbol{x}}}(k|k)$ can be computed from (27). Substituting (32) into (29)-(31) gives

$$\begin{aligned} \bar{\mathbf{L}}(k) &= \mathbf{P}_{\boldsymbol{x}}(k|j)\mathbf{H}^{\mathsf{T}}(k)\mathbf{T}^{\mathsf{T}} \\ &= \mathbf{L}(k)\mathbf{T}^{\mathsf{T}}, \end{aligned} \tag{33}$$

$$\begin{aligned} \bar{\mathbf{S}}(k) &= \mathbf{T}\mathbf{H}(k)\mathbf{L}(k)\mathbf{T}^{\mathsf{T}} + \mathbf{T}\mathbf{R}(k)\mathbf{T}^{\mathsf{T}} \\ &= \mathbf{T}\mathbf{S}(k)\mathbf{T}^{\mathsf{T}}, \end{aligned} \tag{34}$$

$$\begin{aligned} \bar{\boldsymbol{\nu}}(k) &= \mathbf{T}\boldsymbol{z}(k) - \mathbf{T}\hat{\boldsymbol{z}}(k|j) \\ &= \mathbf{T}\boldsymbol{\nu}(k). \end{aligned} \tag{35}$$

Substituting (33)-(35) into (27) yields

$$\tilde{\tilde{\boldsymbol{x}}}(k|k) = \tilde{\tilde{\boldsymbol{x}}}(k|j) - \mathbf{L}(k)\mathbf{T}^{\mathsf{T}} \cdot [\mathbf{T}\mathbf{S}(k)\mathbf{T}^{\mathsf{T}}]^{-1}\mathbf{T}\boldsymbol{\nu}(k). \tag{36}$$

Recall that $\mathbf{T}$ is the difference operator, which computes the TDOA measurements when the n^{th} receiver references the drawn pseudoranges with respect to an arbitrary SOP number ι_n and has the block diagonal structure (25).

Next, consider the block of $\mathbf{T}$ that corresponds to the n^{th} receiver, which can be written as

$$\mathbf{T}_{\iota_n} = \mathbf{J}_{\iota_n} - \boldsymbol{v}\boldsymbol{e}_{\iota_n}^{\mathsf{T}}, \tag{37}$$

where $\mathbf{J}_{\iota_n} \in \mathbb{R}^{[(M-1)\times M]}$ is formed by removing the ι_n^{th} row from an identity matrix,

$$\boldsymbol{v} \triangleq [1, \ldots, 1]^{\mathsf{T}} \in \mathbb{R}^{(M-1)},$$

and $\boldsymbol{e}_{\iota_n}$ denotes the ι_n^{th} standard basis vector of appropriate dimension consisting of a 1 in the ι_n^{th} element and zeros elsewhere. From (37), it is easy to verify that $\mathbf{T}_{\iota_n} \in \mathbb{R}^{[(M-1)\times M]}$ is full row-rank and that $\mathbf{1} \triangleq \left[\boldsymbol{v}^{\mathsf{T}}, 1\right]^{\mathsf{T}}$ is a basis for the null space of $\mathbf{T}_{\iota_n}$; therefore,

$$\begin{aligned} \mathbf{0} \;&=\; \mathbf{T}_{\iota_n}\mathbf{1} = \sum_{i=1}^{M} \mathbf{T}_{\iota_n}\boldsymbol{e}_i \\ &\Rightarrow -\sum_{\substack{i=1 \\ i\neq q}}^{M} \boldsymbol{t}_{\iota_n,i} = \boldsymbol{t}_{\iota_n,q}, \quad \forall\, q \in [1, \ldots, M], \end{aligned} \tag{38}$$

where $\boldsymbol{t}_{\iota_n,i} \triangleq \mathbf{T}_{\iota_n}\boldsymbol{e}_i$ and $\boldsymbol{t}_{\iota_n,q} \triangleq \mathbf{T}_{\iota_n}\boldsymbol{e}_q$ denote the i^{th} and q^{th} column of $\mathbf{T}_{\iota_n}$, respectively. Partitioning $\mathbf{T}_{\iota_n}$ into columns yields

$$\begin{aligned} \mathbf{T}_{\iota_n} &= \left[\boldsymbol{t}_{\iota_n,1}, \ldots, \boldsymbol{t}_{\iota_n,M}\right] \\ &= \left[\mathbf{T}_{\iota_n,1:M-1}, \boldsymbol{t}_{\iota_n,M}\right], \end{aligned} \tag{39}$$

where $\mathbf{T}_{\iota_n,1:M-1}$ denotes the matrix consisting of the columns $\boldsymbol{t}_{\iota_n,1}$ through $\boldsymbol{t}_{\iota_n,M-1}$. Substituting the left-hand side of (38) for $q \equiv M$ into the last column of (39) gives

$$\mathbf{T}_{\iota_n} = \left[\mathbf{T}_{\iota_n,1:M-1}, -\sum_{i=1}^{M-1} \boldsymbol{t}_{\iota_n,i}\right]. \tag{40}$$

Next, consider the difference operator matrix

$$\mathbf{T}' = \operatorname{diag}\left[\mathbf{T}_{\iota'_1}, \ldots \mathbf{T}_{\iota'_N}\right], \tag{41}$$

which forms the set of TDOA measurements when the n^{th} receiver uses SOP ι'_n as its reference, where $\iota'_n \in [1, \ldots, M]$. Proceeding in a similar manner that was used to write $\mathbf{T}_{\iota_n}$ as (40), it is straightforward to show that $\mathbf{T}_{\iota'_n}$ can be written as

$$\mathbf{T}_{\iota'_n} = \left[\mathbf{T}_{\iota'_n,1:M-1}, -\sum_{i=1}^{M-1} \boldsymbol{t}_{\iota'_n,i}\right]. \tag{42}$$

Note that since $\mathbf{T}_{\iota_n}$ and $\mathbf{T}_{\iota'_n}$ are full row-rank, the matrices $\mathbf{T}_{\iota_n,1:M-1}$ and $\mathbf{T}_{\iota'_n,1:M-1}$ are square and invertible; therefore, there exists a matrix $\mathbf{E}_n$, such that

$$\mathbf{T}_{\iota'_n,1:M-1} = \mathbf{E}_n^{-1}\mathbf{T}_{\iota_n,1:M-1}. \tag{43}$$

From (43), the columns of $\mathbf{T}_{\iota'_n,1:M-1}$ are related to the columns of $\mathbf{T}_{\iota_n,1:M-1}$ through

$$\boldsymbol{t}_{\iota'_n,i} = \mathbf{E}_n^{-1}\boldsymbol{t}_{\iota_n,i}, \quad i = 1, \ldots, M-1. \tag{44}$$

Substituting the righthand side of (43) and (44) into the righthand side of (42) yields

$$\begin{aligned} \mathbf{T}_{\iota'_n} &= \left[\mathbf{E}_n^{-1}\mathbf{T}_{\iota_n,1:M-1}, -\mathbf{E}_n^{-1}\sum_{i=1}^{M-1} \boldsymbol{t}_{\iota_n,i}\right] \\ &= \mathbf{E}_n^{-1}\mathbf{T}_{\iota_n}. \end{aligned} \tag{45}$$

The relationship between $\mathbf{T}'$ and $\mathbf{T}$ can be found by substituting (45) into (41) for $n = 1, \ldots, N$, which gives

$$\begin{aligned} \mathbf{T}' &= \operatorname{diag}\left[\mathbf{E}_1^{-1}\mathbf{T}_{\iota_1}, \ldots, \mathbf{E}_N^{-1}\mathbf{T}_{\iota_N}\right] \\ &= \mathbf{E}^{-1}\mathbf{T}, \end{aligned} \tag{46}$$

where $\mathbf{E}^{-1} \triangleq \operatorname{diag}\left[\mathbf{E}_1^{-1}, \ldots, \mathbf{E}_N^{-1}\right]$. Solving (46) for $\mathbf{T}$ and substituting into (36) gives

$$\begin{aligned} \tilde{\tilde{\boldsymbol{x}}}(k|k) &= \tilde{\tilde{\boldsymbol{x}}}(k|j) - \mathbf{L}(k)\mathbf{T}'^{\mathsf{T}}\mathbf{E}^{\mathsf{T}} \\ &\quad \cdot [\mathbf{E}\mathbf{T}'\mathbf{S}(k)\mathbf{T}'^{\mathsf{T}}\mathbf{E}^{\mathsf{T}}]^{-1}\mathbf{E}\mathbf{T}'\boldsymbol{\nu}(k) \\ &= \tilde{\tilde{\boldsymbol{x}}}(k|j) - \mathbf{L}(k)\mathbf{T}'^{\mathsf{T}}\mathbf{E}^{\mathsf{T}} \\ &\quad \cdot \mathbf{E}^{-\mathsf{T}}[\mathbf{T}'\mathbf{S}(k)\mathbf{T}'^{\mathsf{T}}]^{-1}\mathbf{E}^{-1}\mathbf{E}\mathbf{T}'\boldsymbol{\nu}(k) \\ &= \tilde{\tilde{\boldsymbol{x}}}'(k|k), \end{aligned} \tag{47}$$

where $\tilde{\tilde{\boldsymbol{x}}}'(k|k)$ is the estimation error correction when the difference operator matrix $\mathbf{T}'$ is used. The last step in (47) follows from $\tilde{\tilde{\boldsymbol{x}}}(k|j) = \tilde{\tilde{\boldsymbol{x}}}'(k|j)$, since they only depend on IMU data, making (47) take the same form as (36), except that $\mathbf{T}$ is replaced with $\mathbf{T}'$.

Next, consider the EKF Riccati equation, which governs the time-evolution of the estimation error covariance

$$\begin{aligned} \mathbf{P}_{\tilde{\boldsymbol{x}}}(j+\kappa|j) = \mathbf{F}\big\{&\mathbf{P}_{\tilde{\boldsymbol{x}}}(j|j-\kappa) - \mathbf{P}_{\tilde{\boldsymbol{x}}}(j|j-\kappa)\bar{\mathbf{H}}^{\mathsf{T}}(j) \\ &\cdot \left[\bar{\mathbf{H}}(j)\mathbf{P}_{\tilde{\boldsymbol{x}}}(j|j-\kappa)\bar{\mathbf{H}}^{\mathsf{T}}(j) + \bar{\mathbf{R}}(j)\right]^{-1} \\ &\cdot \bar{\mathbf{H}}(j)\mathbf{P}_{\tilde{\boldsymbol{x}}}(j|j-\kappa)\big\}\mathbf{F}^{\mathsf{T}} + \mathbf{Q}^{+}(j+\kappa, j), \end{aligned}$$

where the time arguments $(j+\kappa, j)$ have been dropped from $\mathbf{F}$ to simplify the notation. Substituting (32) into $\bar{\mathbf{H}}$ and using the relationship found in (45) gives

$$\begin{aligned} &\mathbf{P}_{\tilde{\boldsymbol{x}}}(j+\kappa|j) \\ &= \mathbf{F}\big\{\mathbf{P}_{\tilde{\boldsymbol{x}}}(j|j-\kappa) - \mathbf{P}_{\tilde{\boldsymbol{x}}}(j|j-\kappa)\mathbf{H}^{\mathsf{T}}(j)\mathbf{T}^{\mathsf{T}} \\ &\quad \cdot \left[\mathbf{T}\mathbf{H}(j)\mathbf{P}_{\tilde{\boldsymbol{x}}}(j|j-\kappa)\mathbf{H}^{\mathsf{T}}(j)\mathbf{T}^{\mathsf{T}} + \mathbf{T}\mathbf{R}(j)\mathbf{T}^{\mathsf{T}}\right]^{-1} \\ &\quad \cdot \mathbf{T}\mathbf{H}(j)\mathbf{P}_{\tilde{\boldsymbol{x}}}(j|j-\kappa)\big\}\mathbf{F}^{\mathsf{T}} + \mathbf{Q}^{+}(j+\kappa, j) \\ &= \mathbf{F}\big\{\mathbf{P}_{\tilde{\boldsymbol{x}}}(j|j-\kappa) - \mathbf{P}_{\tilde{\boldsymbol{x}}}(j|j-\kappa)\mathbf{H}^{\mathsf{T}}(j)\mathbf{T}'^{\mathsf{T}}\mathbf{E}^{\mathsf{T}} \\ &\quad \cdot \mathbf{E}^{-\mathsf{T}}\left[\mathbf{T}'\mathbf{H}(j)\mathbf{P}_{\tilde{\boldsymbol{x}}}(j|j-\kappa)\mathbf{H}^{\mathsf{T}}(j)\mathbf{T}'^{\mathsf{T}} + \mathbf{T}'\mathbf{R}(j)\mathbf{T}'^{\mathsf{T}}\right]^{-1}\mathbf{E}^{-1} \\ &\quad \cdot \mathbf{E}\mathbf{T}'\mathbf{H}(j)\mathbf{P}_{\tilde{\boldsymbol{x}}}(j|j-\kappa)\big\}\mathbf{F}^{\mathsf{T}} + \mathbf{Q}^{+}(j+\kappa, j) \\ &= \mathbf{P}_{\tilde{\boldsymbol{x}}'}(j+\kappa|j), \end{aligned}$$

where $\mathbf{P}_{\tilde{\boldsymbol{x}}'}(j+\kappa|j)$ is the prediction error covariance when the difference operator matrix $\mathbf{T}'$ is used. □

B. TOA Versus TDOA

In this subsection, it is shown that fusing TOA measurements from unknown SOPs produces a less than or equal (in a positive semi-definite sense) position estimation error covariance matrix for each navigating vehicle than fusing TDOA measurements.

Theorem 2: Consider an environment comprising N receivers and M unknown SOPs with arbitrary: (i) receiver and SOP clock qualities (i.e., arbitrary $\{\mathbf{Q}_{\text{clk,r},n}\}_{n=1}^{N}$ and $\{\mathbf{Q}_{\text{clk,sop},m}\}_{m=1}^{M}$), (ii) geometric configurations, and (iii) measurement noise covariance (i.e., $\mathbf{R} \succ \mathbf{0}$, but not

necessarily diagonal). The EKF-based CIRSLAM that fuses pseudoranges with a TOA fashion yields a less than or equal (in a positive semi-definite sense) position estimation error covariance for each of the navigating vehicles than a TDOA fashion.

Proof: Define the correction (measurement update) estimation error covariance associated with the n^{th} receiver's position for fusing TOA measurements at time-step k as

$$\mathbf{P}_{\boldsymbol{r}_{b_n}}(k|k) \triangleq \Upsilon_n \mathbf{P}_{\boldsymbol{x}}(k|k)\Upsilon_n^{\mathsf{T}} \tag{48}$$

and the correction (measurement update) estimation error covariance associated with the n^{th} receiver's position for fusing TDOA measurements at time-step k as

$$\begin{aligned}\mathbf{P}_{\bar{\boldsymbol{r}}_{b_n}}(k|k) &\triangleq \Upsilon_n \mathbf{P}_{\bar{\boldsymbol{x}}}(k|k)\Upsilon_n^{\mathsf{T}},\\ \Upsilon_n &\triangleq \left[\mathbf{0}_{3\times\gamma_{n,1}},\, \mathbf{I}_{3\times 3},\, \mathbf{0}_{3\times\gamma_{n,2}}\right],\end{aligned} \tag{49}$$

where $\gamma_{n,1} \triangleq 17n - 14$ and $\gamma_{n,2} \triangleq 17(N-n) + 5M - 11$. Substituting (18) and (28) into $\mathbf{P}_{\boldsymbol{x}}(k|k)$ and $\mathbf{P}_{\bar{\boldsymbol{x}}}(k|k)$ in (48) and (49), respectively, and differencing yields

$$\begin{aligned}&\mathbf{P}_{\bar{\boldsymbol{r}}_{b_n}}(k|k) - \mathbf{P}_{\boldsymbol{r}_{b_n}}(k|k)\\ &\quad= \Upsilon_n\left[\mathbf{L}(k)\mathbf{S}^{-1}(k)\mathbf{L}^{\mathsf{T}}(k) - \bar{\mathbf{L}}(k)\bar{\mathbf{S}}^{-1}(k)\bar{\mathbf{L}}^{\mathsf{T}}(k)\right]\Upsilon_n^{\mathsf{T}}.\end{aligned} \tag{50}$$

Note that the prediction error covariances $\mathbf{P}_{\boldsymbol{x}}(k|j)$ and $\mathbf{P}_{\bar{\boldsymbol{x}}}(k|j)$ are only a function of the IMU data, making them independent of the information fusion type, i.e., $\mathbf{P}_{\boldsymbol{x}}(k|j) = \mathbf{P}_{\bar{\boldsymbol{x}}}(k|j)$; therefore, they have canceled and did not appear in (50). Substituting (33) and (34) into (50) gives

$$\begin{aligned}&\mathbf{P}_{\bar{\boldsymbol{r}}_{b_n}}(k|k) - \mathbf{P}_{\boldsymbol{r}_{b_n}}(k|k)\\ &\quad= \Upsilon_n\big[\mathbf{L}(k)\mathbf{S}^{-1}(k)\mathbf{L}^{\mathsf{T}}(k)\\ &\qquad- \mathbf{L}(k)\mathbf{T}^{\mathsf{T}}\left(\mathbf{T}\mathbf{S}(k)\mathbf{T}^{\mathsf{T}}\right)^{-1}\mathbf{T}^{\mathsf{T}}\mathbf{L}^{\mathsf{T}}(k)\big]\Upsilon_n^{\mathsf{T}}\\ &\quad= \Upsilon_n\mathbf{L}(k)\big[\mathbf{S}^{-1}(k) - \mathbf{T}\left(\mathbf{T}\mathbf{S}(k)\mathbf{T}^{\mathsf{T}}\right)^{-1}\mathbf{T}^{\mathsf{T}}\big]\mathbf{L}^{\mathsf{T}}(k)\Upsilon_n^{\mathsf{T}}.\end{aligned} \tag{51}$$

Define the matrices

$$\mathbf{A}(k) \triangleq \mathbf{S}_c(k)\mathbf{T}^{\mathsf{T}} \in \mathbb{R}^{NM\times N(M-1)}, \tag{52}$$

$$\mathbf{B}_n(k) \triangleq \Upsilon_n\mathbf{L}(k)\mathbf{S}_c^{-1}(k) \in \mathbb{R}^{3\times NM}, \quad n = 1,\ldots,N, \tag{53}$$

where $\mathbf{S}_c$ is the Cholesky decomposition of $\mathbf{S}$, i.e., $\mathbf{S} = \mathbf{S}_c\mathbf{S}_c^{\mathsf{T}}$. Since $\mathbf{S}$ is symmetric positive-definite, $\mathbf{S}_c$ is unique and invertible. Substituting (52) and (53) into (51) yields

$$\begin{aligned}&\mathbf{P}_{\bar{\boldsymbol{r}}_{b_n}}(k|k) - \mathbf{P}_{\boldsymbol{r}_{b_n}}(k|k)\\ &\quad= \mathbf{B}_n(k)\left[\mathbf{I}_{NM\times NM} - \mathbf{A}(k)\left[\mathbf{A}^{\mathsf{T}}(k)\mathbf{A}(k)\right]^{-1}\mathbf{A}^{\mathsf{T}}(k)\right]\mathbf{B}_n^{\mathsf{T}}(k),\end{aligned} \tag{54}$$

Define the matrix

$$\Omega(k) \triangleq \mathbf{A}(k)\left[\mathbf{A}^{\mathsf{T}}(k)\mathbf{A}(k)\right]^{-1}\mathbf{A}^{\mathsf{T}}(k). \tag{55}$$

Substituting (55) into (54) gives

$$\mathbf{P}_{\bar{\boldsymbol{r}}_{b_n}}(k|k) - \mathbf{P}_{\boldsymbol{r}_{b_n}}(k|k) = \mathbf{B}_n(k)\mathbf{M}(k)\mathbf{B}_n^{\mathsf{T}}(k), \tag{56}$$

where $\mathbf{M}(k) \triangleq \mathbf{I}_{NM\times NM} - \Omega(k)$. Note that,

(i) The matrix $\Omega \in \mathbb{R}^{NM\times NM}$ is an orthogonal projection matrix, since it satisfies $\Omega^2 = \Omega = \Omega^{\mathsf{T}}$. It has $N(M-1)$ eigenvalues of ones and N eigenvalues of zeros, since $\text{rank}(\Omega) = \text{rank}(\mathbf{A}) = N(M-1)$. Therefore, Ω is positive semi-definite.

(ii) The matrix $\mathbf{M}$ is also an orthogonal projection matrix, and its eigenvalues consist of N ones and $N(M-1)$ zeros [53]; therefore, it is positive semi-definite.

It follows from (ii) that

$$\mathbf{B}_n(k)\mathbf{M}(k)\mathbf{B}_n^{\mathsf{T}}(k) \succeq \mathbf{0}. \tag{57}$$

From (56) and (57), it can be concluded that

$$\mathbf{P}_{\bar{\boldsymbol{r}}_{b_n}}(k|k) \succeq \mathbf{P}_{\boldsymbol{r}_{b_n}}(k|k). \tag{58}$$

□

VII. Simulation Results

This section presents simulation results evaluating Theorem 1 and Theorem 2. The simulation settings and EKF initialization settings are described.

A. Simulation Environment and Settings

The simulation environment consists of $N = 4$ UAV-mounted receivers and $M = 6$ SOP transmitters. The receivers were set to have GPS available for the first 50 seconds of their trajectory and then unavailable for the remaining 150 seconds portion of the trajectory. SOP pseudoranges were available for their entire trajectories. The simulated UAV trajectories, SOP transmitters' positions, and the UAVs' positions at the time GPS was set to become unavailable are illustrated in Fig. 3. All simulations were created in MATLAB. The vehicle trajectories were produced via a high-fidelity simulator described in [30], which has been validated against real vehicle telemetry over a 10-year period in industry. Sensor data was simulated by the authors according to the models in this paper. The following describes the methods used to produce the simulated data.

1) UAVs' Trajectories: The UAVs' simulated trajectories were generated using a standard six degree of freedom (6DoF) kinematic model for airplanes [51]. Each vehicle performed the same maneuvers, which included the following segments conducted in succession over a 200 second period: 10 second straight and level linear acceleration along the direction of travel; 5 degree pitching climb for 30 seconds; 22 second straight and level linear velocity, while rolling to 60 degrees; five 60 degree left-banking turns. These trajectory segments were chosen because they collectively excite all 6DoF of the UAVs, i.e., both horizontal and vertical directions and all three angles (roll, pitch, and yaw), allowing the TOA and TDOA information fusion strategies to be studied under various maneuvers.

2) IMU Data: The gyroscope and accelerometer data were generated at 100 Hz using the simulated vehicles' accelerations and rotation rates through equations (4) and (5), respectively. The evolution of each vehicle's gyroscope and accelerometer biases were generated according to equations (6) and (7), respectively, using driving process noise with spectra $\mathbf{S}_{\boldsymbol{w}_{\text{gyr}},n} \equiv (10^{-8})\cdot\mathbf{I}_{3\times 3}$ and $\mathbf{S}_{\boldsymbol{w}_{\text{acc}},n} \equiv 10^{-8}\cdot\mathbf{I}_{3\times 3}$, respectively. The power of the corrupting white noise was

set to correspond to a consumer-grade IMU. IMUs of this quality typically state the noise values in terms of accumulated noise. Each axis of the IMU was set to have an accumulated noise of 0.3 deg/s and 2.5 milligravities for the gyroscope and accelerometer, respectively. These spectra are mapped to the discrete-time noise covariances $\mathbf{Q}_{\boldsymbol{n}_{\text{gyr},n}}$, $\mathbf{Q}_{\boldsymbol{n}_{\text{acc},n}}$, $\mathbf{Q}_{\boldsymbol{w}_{\text{gyr},n}}$, and $\mathbf{Q}_{\boldsymbol{w}_{\text{acc},n}}$ through the equations provided in Appendix A.

3) Receiver Clock: Each UAV-mounted receiver was set to be equipped with a typical temperature-compensated crystal oscillator (TCXO), with parameters $\{h_{0,r_n}, h_{-2,r_n}\}_{n=1}^{4} = \{9.4 \times 10^{-20}, 3.8 \times 10^{-21}\}$. These parameters are used to compute the process noise covariance $\mathbf{Q}_{\text{clk,r},n}$ that drive the receiver clock dynamics found according to equation (1).

4) GPS Pseudoranges: GPS L1 C/A pseudoranges were generated at 1 Hz according to equation (10). The position of each GPS satellite was generated by producing their orbits using Receiver Independent Exchange (RINEX) files, downloaded from a Continuously Operating Reference Station (CORS) server [54]. Pseudorange from eleven GPS satellites ($L = 11$) were set to be available for $t \in [0, 50)$ seconds, and unavailable ($L = 0$) for $t \in [50, 200]$ seconds. The GPS pseudorange measurement noise terms were set to be independent from each other with measurement noise variance computed according to [55]

$$ {}^{n}\sigma^2_{\text{sv},l,j} = \frac{c^2\, t_{\text{eml}}\, B_{\text{DLL}}\, T_c^2\, \sigma_s^2}{2^n (C/N_0)_{l,j}} \left[1 + \frac{1}{T_{\text{CO}}{}^n (C/N_0)_{l,j}}\right], \quad (59) $$

where $t_{\text{eml}} \equiv 0.5$ chips is the early-minus-late correlator spacing, $B_{\text{DLL}} \equiv 0.05$ Hz is the delay lock loop (DLL) bandwidth, $T_c \equiv 1/(1.023 \times 10^6)$ s is the chip duration, ${}^{n}(C/N_0)_{l,j}$ (in Hz) is the time-varying received carrier-to-noise ratio at UAV n from satellite l, which was derived from the RINEX files, $\sigma_s \equiv 17$ is a scaling parameter to account for unmodeled errors, and $T_{CO} \equiv 10$ ms is the coherent integration time. Equation (59) is the model used in this work; however, other models may be used. Another common model often employed is the scaled C/N_0 - elevation model [56]. The point at which GPS was cut off is illustrated as a red 'X' in Fig. 3.

5) SOP Pseudoranges: Pseudoranges were generated to the SOPs at 5 Hz according to equation (9). The evolution of each SOP's clock bias was modeled according to the dynamics discussed in Subsection IV-A, using parameters that correspond to a typical oven-controlled crystal oscillator (OCXO), with $\{h_{0,\text{sop},m}, h_{-2,\text{sop},m}\}_{m=1}^{6} = \{8 \times 10^{-20}, 4 \times 10^{-23}\}$. The SOP transmitters' positions $\{\boldsymbol{r}_{\text{sop},m}\}_{m=1}^{6}$ were surveyed from cellular tower locations in downtown Los Angeles, California, USA. The SOP pseudorange measurement noise terms were set to be independent with a measurement noise variance according to (59), except that $t_{\text{eml}} \equiv 1$, ${}^{n}\sigma^2_{\text{sv},l,j}$ is replaced with ${}^{n}\sigma^2_{\text{sop},m,j}$, $T_c \equiv 1/(1.2288 \times 10^6)$, $\sigma_s \equiv 22$, $T_{CO} \equiv 1/37.5$ s, and the carrier-to-noise ratio ${}^{n}(C/N_0)_{m,j}$ is replaced with a time-varying log-distance path loss model [57]

$$ {}^{n}(C/N_0)'_{m,j} = P_0 - 10\gamma \cdot \log_{10}(d(j)/D_0), $$
$$ {}^{n}(C/N_0)_{m,j} = 10^{[{}^{n}(C/N_0)'_{m,j}/10]}, $$

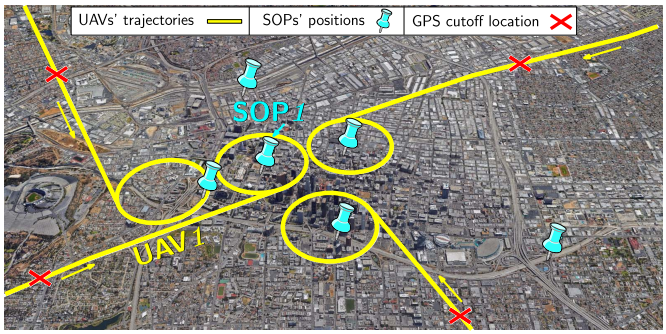

Fig. 3. True trajectories the UAVs traversed (yellow), SOP transmitters' positions (blue pins), and the UAVs' positions at the time GPS was cut off (red).

where $P_0 \equiv 56$ dB-Hz is a calibration carrier-to-noise ratio at a distance $D_0 \equiv 1400$ m, $d(j) \triangleq \|{}^{e}\boldsymbol{r}_b(j) - {}^{e}\boldsymbol{r}_{\text{sop},m}\|_2$, and $\gamma \equiv 2$ is the path loss exponent. The calibration values P_0 and D_0 are values commonly observed by the authors during experimental campaigns [21], [58]. The SOP pseudorange measurement noise variance computation assumes that the correlation function within the DLL is equivalent to GPS. This is a reasonable assumption for cellular code division multiple access (CDMA) signals, when t_{eml} is between 0.8 and 1.25 chips. More sophisticated models for cellular CDMA are discussed in [59] and for long-term evolution (LTE) are discussed in [23]. If at any point in time pseudoranges become faulty or there is a sudden significant jump due to multipath from any of the SOPs, then the pseudoranges associated with that SOP should be temporarily excluded using a receiver autonomous integrity monitoring (RAIM) framework for SOPs [58]. For moderate multipath-induced biases, one can apply well-known multipath mitigation techniques [28], [60]–[63].

B. EKF-Based CIRSLAM Filter Initialization

The initial estimates (at $t = 0$ seconds) of the UAVs' states were initialized by drawing a random error vector from a multivariate Gaussian distribution and then adding the error to the "ground truth" state at $t = 0$. This initialization method is used instead of directly drawing the state estimate to deal with the quaternion initialization, which requires special handling. This method is described in the next three steps. First, the random error for each UAV was drawn according to

$$ \tilde{\boldsymbol{x}}_{\text{r},n}(0|0) \sim \mathcal{N}\left[\mathbf{0}_{17\times 1},\, \mathbf{P}_{\boldsymbol{x}_{\text{r},n}}(0|0)\right] $$
$$ \mathbf{P}_{\boldsymbol{x}_{\text{r},n}}(0|0) \triangleq \text{diag}\left[\mathbf{P}_{\boldsymbol{x}_{\text{ins},n}}(0|0),\, \mathbf{P}_{\boldsymbol{x}_{\text{clk,r}}}(0|0)\right] $$
$$ \mathbf{P}_{\boldsymbol{x}_{\text{ins},n}}(0|0) \equiv \text{diag}\left[(10^{-2}) \cdot \mathbf{I}_{3\times 3}, 9 \cdot \mathbf{I}_{3\times 3}, \mathbf{I}_{3\times 3}, (10^{-4}) \cdot \mathbf{I}_{6\times 6}\right] $$
$$ \mathbf{P}_{\boldsymbol{x}_{\text{clk,r},n}}(0|0) \equiv \text{diag}\,[9,\, 1], $$

were $\boldsymbol{a} \sim \mathcal{N}(\boldsymbol{\mu}, \mathbf{C})$ indicates that $\boldsymbol{a}$ is Gaussian-distributed with mean $\boldsymbol{\mu}$ and covariance $\mathbf{C}$. Second, to produce the initial quaternion estimate, two approaches are common and may be used. The small angle errors may be used to create a rotation matrix, which can then be converted to quaternion and multiplied by the true angle in order to produce

a new quaternion, which will serve as the initial estimate. Alternatively, the resulting angle error $\boldsymbol{\theta} \in \mathbb{R}^3$, which are the first three elements of $\tilde{\boldsymbol{x}}_{\mathrm{r},n}$, may be mapped to an error quaternion $\tilde{\boldsymbol{q}}_n \in \mathbb{R}^4$, which are then applied to the true state according to the equations discussed in Appendix C of [30]. Third, to produce initial estimates of the remaining states, the remaining error components of $\tilde{\boldsymbol{x}}_{\mathrm{r},n}$ are applied to the true states as standard additive error.

The SOPs' state estimates were initialized according to $\hat{\boldsymbol{x}}_{\mathrm{sop},m}(0|0) \sim \mathcal{N}\left[\boldsymbol{x}_{\mathrm{sop},m}(0), \mathbf{P}_{\mathrm{sop}}(0|0)\right]$, for $m = 1, \ldots, M$, where $\boldsymbol{x}_{\mathrm{sop},m}(0) \equiv \left[\boldsymbol{r}_{\mathrm{sop},m}^{\mathsf{T}}, 10^4, 10\right]^{\mathsf{T}}$, and $\mathbf{P}_{\mathrm{sop}}(0|0) \equiv (10^4) \cdot \mathrm{diag}\left[\mathbf{I}_{3\times 3}\, 0.1,\ 0.01\right]$. This initialization scheme is used in simulation to ensure consistent initial priors in the EKF. In practice, if the initial SOPs' states are completely unknown, then a random position for each SOP may be drawn in the vicinity of the UAVs with a large enough uncertainty to encompass all possible points that a signal could be received from. The clock states may be initialized to zero with a large uncertainty. As long as there are enough vehicle's or the vehicles are moving, the position and clock states of the SOPs are observable. Observability conditions are thoroughly analyzed in [32], [64], [65].

If a new vehicle needs to be added to the EKF after initialization, the state vector could be augmented with the new vehicle's 18 states and the covariance matrix would gain a 17×17 block representing the uncertainty in those states. The off-diagonal components of the covariance matrix would be populated with zeros, since no correlation exists at the first instance. These off-diagonal elements would begin to populate as EKF measurement updates are processed. Alternatively, to avoid augmenting the state vector with new states, factor graphs could be explored in future research for this problem [66], [67].

C. TDOA SOP Reference Selection

This subsection presents simulation results evaluating Theorem 1. To do this, the produced UAVs' position estimation error covariances are shown to be independent of the chosen SOP reference when the UAVs use the TDOA information fusion strategy under various clock and measurement qualities and UAV-to-SOP geometries. Four different scenarios were studied, where each scenario has different simulation settings:

- Scenario A: Settings described in Subsection VII-A.
- Scenario B: Equivalent to Scenario A, except that SOP 2 was set to be equipped with a worst TCXO, with $\{h_{0,\mathrm{sop},2}, h_{-2,\mathrm{sop},2}\} = \{2 \times 10^{-19}, 2 \times 10^{-20}\}$ and the other five SOPs were set to be equipped with a best OCXO, with $\{h_{0,\mathrm{sop},m}, h_{-2,\mathrm{sop},m}\}_{m=1}^{6} \backslash 2 = \{2.6 \times 10^{-22}, 4 \times 10^{-23}\}$.
- Scenario C: Equivalent to Scenario A, except that the measurement noise standard deviation scaling parameter for SOP 2 was set to $\sigma_s \equiv 10$.
- Scenario D: Equivalent to Scenario A, except that the simulation environment was set to be in Portland, Oregon, USA. The SOP locations and UAV trajectories are illustrated in Fig. 4. To avoid cluttering the figure, only the trajectories for UAV 1 and 2 are shown. The trajectories for UAV 3 and 4 had the same profiles as UAV 1 and 2, respectively.

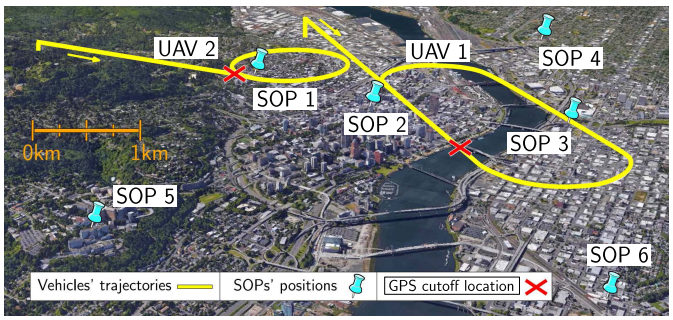

Fig. 4. Scenario D environment showing: true trajectories the UAVs traversed (yellow), SOP transmitters' positions (blue pins), and the UAVs' positions at the time GPS was cut off (red).

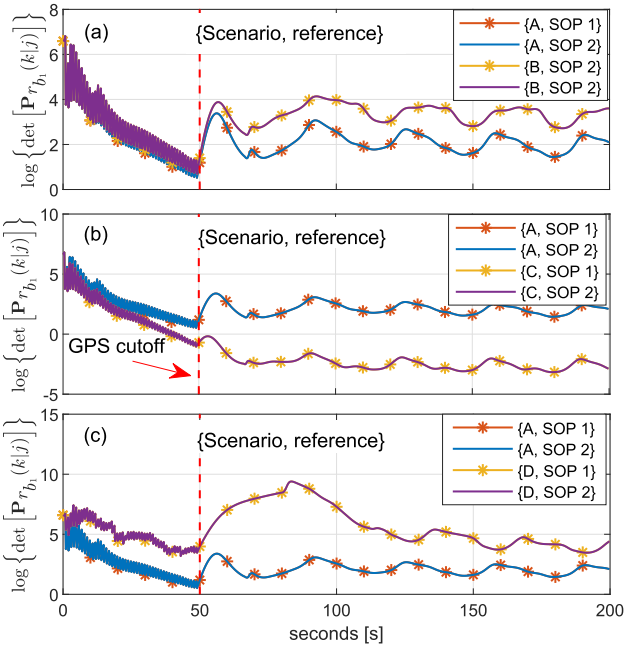

Fig. 5. The logarithm of the determinant of the position estimation error covariance of UAV 1 for using the TDOA information fusion strategy with different SOP reference selection.

For each of the four scenarios, two runs were conducted. In the first run, the UAVs selected SOP 1 as the reference. In the second run, the UAVs selected SOP 2. The EKF for all eight runs were initialized according to the procedure discussed in Subsection VII-B. Fig. 5 illustrates the logarithm of the determinant of the estimation error covariance of the same UAV's position states, $\log\left\{\det\left[\mathbf{P}_{\boldsymbol{r}_{b_1}}\right]\right\}$, which is related to the volume of the uncertainty ellipsoid [68].

Note from Fig. 5 that the two logdet trajectories in each scenario (each trajectory corresponding to a particular SOP reference selection) are on top of each other. These are representative results. The estimation error trajectories and corresponding covariances for the other three UAVs exhibited the same behavior, indicating that the estimation error covariances

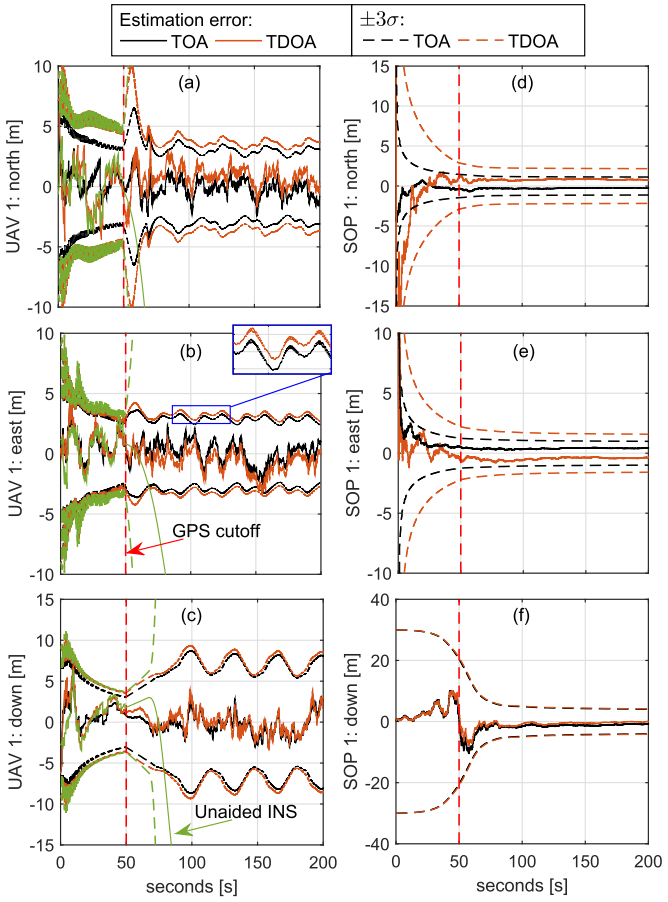

Fig. 6. Estimation error trajectories and $\pm 3\sigma$ bounds for the (1) TOA and (2) TDOA with SOP referencing information fusion strategies for the environment depicted in Fig. 3. (a)-(c) Correspond to UAV 1 north, east, and down position errors, respectively. (d)-(f) Correspond to SOP 1 north, east, and down position errors, respectively. The red dotted line marks the time GPS pseudoranges were set to become unavailable ($L = 0$).

are independent of the SOP reference selection, as established in Theorem 1.

D. TOA Versus TDOA Performance Comparison

This subsection presents simulation results evaluating Theorem 2. This theorem was evaluated by comparing the UAVs' resulting position estimation error covariances that are produced when using (i) TOA and (ii) TDOA with SOP referencing, described in Subsection V-E and Subsection V-F, respectively. For each strategy, the simulation and EKF initialization settings described in Subsection VII-A and Subsection VII-B, respectively, were used. Errors for a traditional tightly-coupled GPS-aided INS are also provided for a comparative analysis.

Fig. 6 shows the resulting estimation error trajectories and corresponding ± 3 times the EKF-produced estimation error standard deviations ($\pm 3\sigma$) for both strategies for the north, east, and down position states for UAV 1 and SOP 1. Fig. 7 illustrates $\log\left\{\det\left[\mathbf{P}_{\boldsymbol{r}_{b_1}}\right]\right\}$, for the same UAV. Note that TDOA measurements were produced using SOP 2 as the reference selection. The results were *identical* for choosing any other SOP as a reference, as expected from Theorem 1.

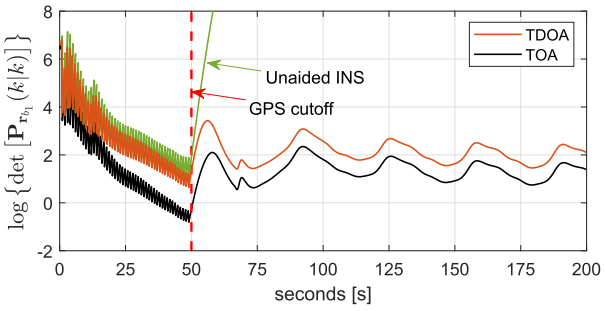

Fig. 7. The logarithm of the determinant of the position estimation error covariance of UAV 1 for the environment depicted in Fig. 3.

The following performance comparison may be concluded from these plots. First, the errors associated with the collaborative SOP-aided INS, regardless of the CIRSLAM information fusion strategy, remained bounded after GPS was cut off, whereas the errors associated with an unaided INS began to diverge as expected. This indicates that if navigating vehicles are sharing and fusing INS information and pseudoranges drawn from SOPs with uncertain states, requirements on their INSs may be relaxed. That is, the cost of the navigation system can be reduced, since lower grade IMUs may still meet positioning accuracy requirements. Second, the TOA information fusion strategy consistently produced lower estimation error variances compared to the TDOA information fusion strategy in all coordinate directions. This indicates that the UAV's position uncertainty in any coordinate direction at any given time is less when SOP TOA measurements are shared and fused than TDOA. Equivalently, the size of the uncertainty ellipsoid of the UAV's position states will be smaller if TOA is used and the difference in size is captured by the distance between in the $\log\left\{\det\left[\mathbf{P}_{\boldsymbol{r}_{b_1}}(k|k)\right]\right\}$ curves illustrated in Fig. 7. Similar behavior of the estimation error uncertainties in the position states was noticed for the other UAVs and SOPs during simulation runs with different realizations of measurement and process noise. These findings support Theorem 2.

To expand on these single run results, an analysis was conducted using four different scenarios to show that the n^{th} vehicle's produced estimation error covariance using TOA, denoted $\mathbf{P}_{\boldsymbol{r}_{b_n}}$, is less than or equal to the estimation error covariance using TDOA, denoted $\mathbf{P}_{\tilde{\boldsymbol{r}}_{b_n}}(k|k)$, regardless of the clock and measurement qualities and the UAV-to-SOP geometries. To this end, each of the four scenarios described in Subsection VII-C was ran five times for 200 seconds each. Each of the four runs within each scenario used a different GPS cutoff time, which was drawn according to a uniform distribution between 50 and 200 seconds. The initial time of 50 seconds was selected as the uniform distribution bound to allow time for INS error initialization. For each run, a point was plotted at each instant k of the minimum eigenvalue of $\mathbf{P}_{\tilde{\boldsymbol{r}}_{b_n}}(k|k) - \mathbf{P}_{\boldsymbol{r}_{b_n}}(k|k)$, denoted $\lambda_{\min}\left[\mathbf{P}_{\tilde{\boldsymbol{r}}_{b_n}}(k|k) - \mathbf{P}_{\boldsymbol{r}_{b_n}}(k|k)\right]$, for each of the UAVs $n = 1, \ldots 4$, where $k = 1, \ldots, 200/T_{\text{sop}}$ and $T_{\text{sop}} = 0.5$. The resulting point cloud is illustrated in Fig. 8.

Note from the point cloud in Fig. 8 that the minimum eigenvalue is always greater than zero, regardless of the

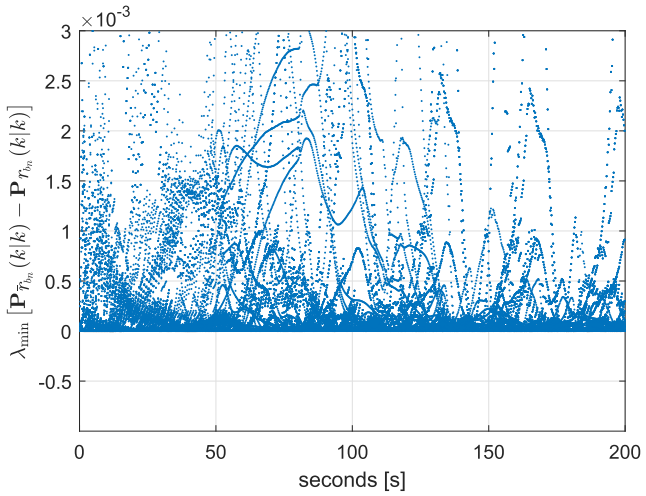

Fig. 8. Minimum eigenvalue of the difference of the position estimation error covariances for using the TDOA and TOA information fusion strategies.

clock quality, measurement quality, or geometry. Therefore, $\mathbf{P}_{\tilde{\boldsymbol{r}}_{b_n}} \succeq \mathbf{P}_{\boldsymbol{r}_{b_n}}$, as expected from Theorem 2.

VIII. Experimental Demonstration

This section presents an experimental demonstration of the TOA and TDOA information fusion strategies using two UAVs equipped with *consumer*-grade IMUs and software-defined radios (SDRs). The following experiment was conducted by collecting the IMU, GPS, and SOP data in the field, after which the communication and fusion of the data was emulated via post-processing in the lab.

A. Hardware and Software Setup

A Consumer-grade L1 GPS active patch antenna [69] and an omnidirectional cellular antenna [70] were mounted on each UAV to acquire and track GPS signals and multiple cellular transmitters, respectively, whose signals were modulated through code division multiple access (CDMA). The GPS and cellular signals were simultaneously downmixed and synchronously sampled via two-channel Ettus® E312 universal software radio peripherals (USRPs). These front-ends fed their data to the Multichannel Adaptive TRansceiver Information eXtractor (MATRIX) SDR, which produced pseudorange measurements from all GPS L1 C/A signals in view and three cellular transmitters at 10 Hz. The IMU data was sampled at 100 Hz from the UAVs' on-board proprietary navigation system, which was developed by Autel Robotics®. Fig. 9 depicts the hardware and software setup and Fig. 10(a) shows the environment.

B. CIRSLAM Initialization and Settings

The CIRSLAM framework was initialized using the following procedure for each of the two results presented in the subsequent subsections. The state vector estimate was initialized according to

$$\hat{\boldsymbol{x}}(0|0) = \left[\hat{\boldsymbol{x}}_{\mathrm{r},1}^{\mathsf{T}}(0|0), \hat{\boldsymbol{x}}_{\mathrm{r},2}^{\mathsf{T}}(0|0), \hat{\boldsymbol{x}}_{\mathrm{sop},1}^{\mathsf{T}}(0|0), \ldots, \hat{\boldsymbol{x}}_{\mathrm{sop},3}^{\mathsf{T}}(0|0)\right]^{\mathsf{T}},$$

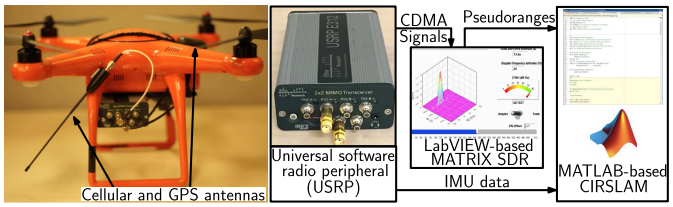

Fig. 9. Experiment hardware setup.

where the estimates of each UAV's orientation ${}^{b_n}_{g}\hat{\boldsymbol{q}}(0|0)$, position $\hat{\boldsymbol{r}}_{b_n}(0|0)$, and velocity $\hat{\dot{\boldsymbol{r}}}_{b_n}(0|0)$ were set to values parsed from the beginning of the UAV's navigation system log files, which were recorded during the trajectory, and the IMU biases $\hat{\boldsymbol{b}}_{\mathrm{gyr},n}$ and $\hat{\boldsymbol{b}}_{\mathrm{acc},n}$ were initialized by averaging 5 seconds of gravity-compensated IMU measurements while the vehicles were stationary and after their IMUs had warmed up. The cellular SOP transmitters' initial state estimates were drawn according to $\hat{\boldsymbol{x}}_{\mathrm{sop},m}(0|0) \sim \mathcal{N}\big(\big[\boldsymbol{r}_{\mathrm{sop},m}^{\mathsf{T}}, \boldsymbol{x}_{\mathrm{clk,sop},m}^{\mathsf{T}}(0)\big]^{\mathsf{T}}, \mathbf{P}_{\mathrm{sop},m}(0|0)\big)$. The true transmitters' positions $\{\boldsymbol{r}_{\mathrm{sop},m}\}_{m=1}^{3}$ were surveyed beforehand and verified using Google Earth. The initial clock bias and drift

$$\boldsymbol{x}_{\mathrm{clk,sop},m}(0) = c\left[\delta t_{\mathrm{sop},m}(0),\ \dot{\delta t}_{\mathrm{sop},m}(0)\right]^{\mathsf{T}} \quad m = 1, \ldots, 3,$$

were solved for by using the initial set of cellular transmitter pseudoranges using equation (9) according to

$$c\delta t_{\mathrm{sop},m}(0) = \|\boldsymbol{r}_{b_n}(0) - \boldsymbol{r}_{\mathrm{sop},m}\| + c\delta t_{\mathrm{r},n}(0) - z_{\mathrm{sop},m}(0),$$
$$c\dot{\delta t}_{\mathrm{sop},m}(0) = [c\delta t_{\mathrm{sop},m}(1) - c\delta t_{\mathrm{sop},m}(0)]/T,$$

where $c\delta t_{\mathrm{sop},m}(1) = \|\boldsymbol{r}_{b_n}(1) - \boldsymbol{r}_{\mathrm{sop},m}\| + c\delta t_{\mathrm{r},n}(1) - {}^{n}z_{\mathrm{sop},m}(1)$ and the receiver's clock bias $c\delta t_{\mathrm{r},n}(0)$ and $c\delta t_{\mathrm{r},n}(1)$ was provided by the GPS receiver while GPS was available.

The corresponding estimation error covariance was initialized according to

$$\begin{aligned}
\mathbf{P}_{\boldsymbol{x}}(0|0) &= \mathrm{diag}\left[\mathbf{P}_{\boldsymbol{x}_{\mathrm{r}}}(0|0), \mathbf{P}_{\boldsymbol{x}_{\mathrm{sop},1}}(0|0), \ldots, \mathbf{P}_{\boldsymbol{x}_{\mathrm{sop},3}}(0|0)\right],\\
\mathbf{P}_{\boldsymbol{x}_{\mathrm{r}}}(0|0) &= \mathrm{diag}\left[\mathbf{P}_{\boldsymbol{x}_{\mathrm{r},1}}(0|0), \mathbf{P}_{\boldsymbol{x}_{\mathrm{r},2}}(0|0)\right],\\
\mathbf{P}_{\boldsymbol{x}_{\mathrm{r},n}}(0|0) &\triangleq \mathrm{diag}\left[\mathbf{P}_{\boldsymbol{x}_{\mathrm{imu},n}}(0|0),\ \mathbf{P}_{\boldsymbol{x}_{\mathrm{clk,r},n}}(0|0)\right]\\
\mathbf{P}_{\boldsymbol{x}_{\mathrm{imu},n}}(0|0) &\equiv \mathrm{diag}\left[(0.1)\cdot\mathbf{I}_{3\times3}, 9\cdot\mathbf{I}_{3\times3}, \mathbf{I}_{3\times3}, (10^{-4})\cdot\mathbf{I}_{6\times6}\right]\\
\mathbf{P}_{\boldsymbol{x}_{\mathrm{clk,r},n}}(0|0) &\equiv \mathrm{diag}\left[0.1,\ 0.01\right] \quad n = 1, 2,\\
\mathbf{P}_{\mathrm{sop},m}(0|0) &\equiv 10^{3}\cdot\mathrm{diag}\left[\mathbf{I}_{3\times3}, 0.3, 0.03\right], \quad m = 1, 2, 3.
\end{aligned}$$

The process noise covariance of the receiver's clock $\mathbf{Q}_{\mathrm{clk,r},n}$ was set to correspond to a typical TCXO. The process noise covariances of the cellular transmitters' clocks were set to correspond to a typical OCXO, which is usually the case for cellular transmitters [71], [72]. The power spectral density matrices associated with the gyroscope and accelerometer noise were set to $\mathbf{S}_{\boldsymbol{n}_{\mathrm{gyr}}} \equiv (7 \times 10^{-4})^2 \cdot \mathbf{I}_{3\times3}$ and $\mathbf{S}_{\boldsymbol{n}_{\mathrm{acc}}} \equiv (5 \times 10^{-4})^2 \cdot \mathbf{I}_{3\times3}$, respectively. The power spectral density matrices associated with the gyroscope and accelerometer bias variations were set to $\mathbf{S}_{\boldsymbol{w}_{\mathrm{gyr}}} \equiv (1 \times 10^{-4})^2 \cdot \mathbf{I}_{3\times3}$ $\mathbf{S}_{\boldsymbol{w}_{\mathrm{acc}}} \equiv (1 \times 10^{-4})^2 \cdot \mathbf{I}_{3\times3}$, whose values were found empirically using raw IMU data. The measurement noise variances $\{{}^{n}\sigma_{\mathrm{sop},m}^{2}\}_{m=1}^{3}$ for UAV $n \in \{1, 2\}$ were time-varying, and calculated according to (59), except that $t_{\mathrm{eml}} \equiv 1$,

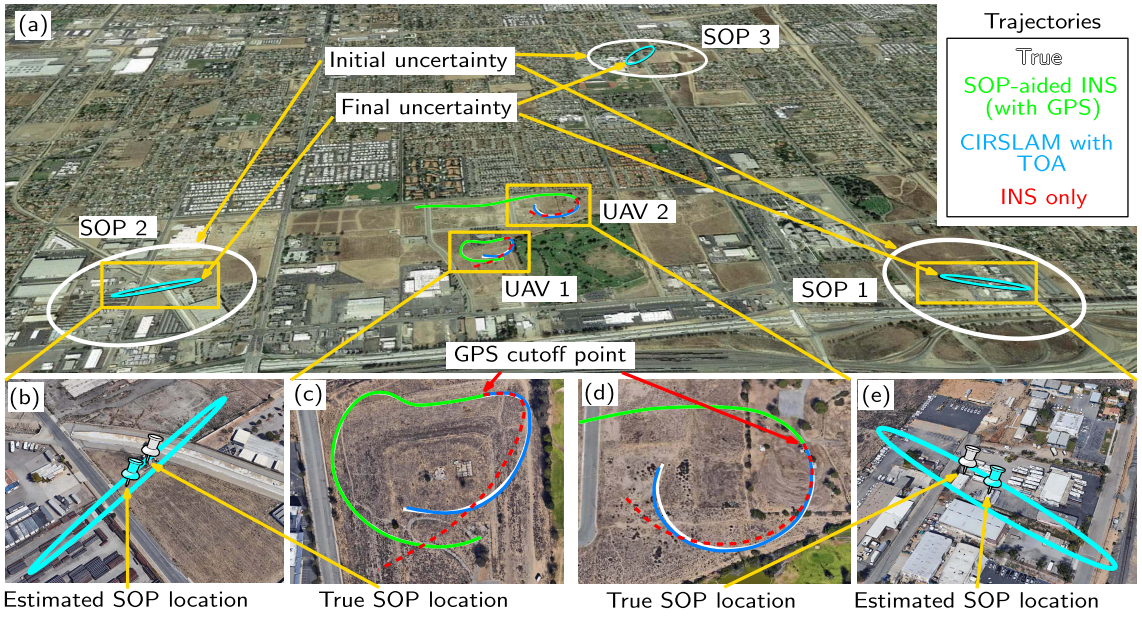

Fig. 10. (a) Experimental environment with three cellular SOPs and two UAVs. (b)-(e) Mapping and navigation results for CIRSLAM with TOA information fusion.

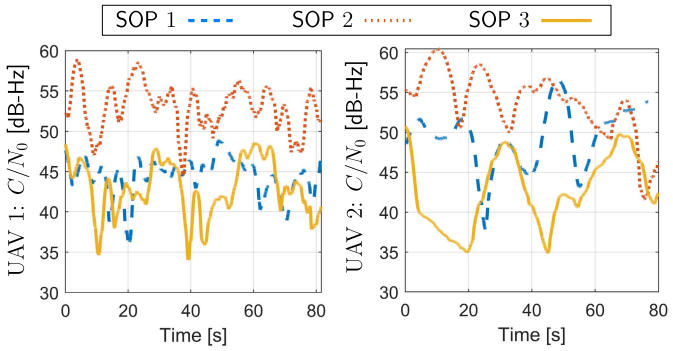

Fig. 11. Time history of received C/N_0 for UAV 1 and UAV 2 from SOP 1, 2, and 3, produced by the MATRIX SDR.

${}^n\sigma^2_{\text{sv},l,j}$ is replaced with ${}^n\sigma^2_{\text{sop},m,j}$, $T_c \equiv 1/(1.2288 \times 10^6)$, $\sigma_s \equiv 10$, $T_{CO} \equiv 1/37.5$ s, and the carrier-to-noise ratios $\{{}^n(C/N_0)_{m,j}\}_{m=1}^3$, $n \in \{1, 2\}$, are replaced with the received carrier-to-noise ratio estimated by the MATRIX SDR, which are plotted in Fig. 11.

C. Experimental Results

Experimental results are presented for three frameworks: (i) CIRSLAM with TOA information fusion, (ii) CIRSLAM with TDOA information fusion, and (iii) for comparative analysis, a traditional GPS-aided INS. The UAVs traversed the white trajectories plotted in Figs. 10(c)–(d), in which GPS was available for the first 50 seconds then unavailable for the last 30 seconds. The north-east root mean squared errors (RMSE) and final errors for all three frameworks for the UAVs are summarized in Table I. Note that collaboratively using SOPs provided around 50 meters of error reduction compared to a GPS-aided INS after 30 seconds of GPS unavailability, whether TOA or TDOA was used. As expected,

TABLE I
ESTIMATION ERRORS: TOA VERSUS TDOA

Framework	GPS-aided INS		CIRSLAM-TOA		CIRSLAM-TDOA	
Vehicle	UAV 1	UAV 2	UAV 1	UAV 2	UAV 1	UAV 2
Pos. RMSE (m)	21.5	18.9	3.1	4.2	3.3	4.4
Final Error (m)	57.3	54.7	4.3	6.0	4.4	6.2

TOA performed slightly better. Collaboration provided around 5 meters of error reduction compared to a *non-collaborating*, single UAV navigating with an SOP-aided INS that used the same IMU and SOP data set [30].

The final estimated transmitter location and corresponding 99^{th}-percentile north-east uncertainty ellipse for two of the transmitters are shown in Fig. 10(b) and Fig. 10(e). The final localization errors for the three transmitters were 9.0, 7.9, and 52.8 m, respectively. Note that the relatively large estimation error of SOP 3 is primarily attributed to relatively large measurement noise compared to the measurement noise associated with SOP 1 and SOP 2. From Fig. 11, it can be seen that the received C/N_0 from SOP 3 at UAV 1 and UAV 2 was lower compared to the C/N_0 from SOP 1 and 2, most of the time. The lower C/N_0 maps to larger estimation error variance, according to (59). The larger measurement variance resulted in a larger final estimation error ellipse, which, nevertheless, contained the true position of SOP 3.

IX. CONCLUSION

This paper developed and studied two information fusion strategies for navigating vehicle's to collaboratively aid their INS's with SOPs: TOA measurements and TDOA measurements with SOP referencing. It was shown that using TOA measurements from SOPs with unknown positions and unknown and unsynchronized clock biases results in a smaller or equal navigating vehicle's position estimation

error covariance than using TDOA measurements, regardless of the selected SOP reference. An approach to share INS data between navigating vehicles in a distributed fashion was discussed, which significantly reduces the amount of data that is required to be transmitted to perform the EKF measurement update. Simulation results supported the analytical findings, which established that using TOA measurements from transmitters with unknown positions and unknown and unsynchronized clock biases results in a smaller or equal (in a positive-definite sense) position estimation error covariance than using TDOA measurements, regardless of the selected SOP reference. Experimental results demonstrated two UAVs navigating with CIRSLAM using TOA measurements from three cellular transmitters in the absence of GPS, which yielded trajectory RMSE reductions of 85.6% for UAV 1 and 77.8% for UAV 2 when compared to unaided INSs.

Appendix
INS State Transition and Process Noise Covariance Matrices

The equivalent rotation matrix $\mathbf{R}[\bar{\boldsymbol{q}}]$ of the quaternion vector $\bar{\boldsymbol{q}} = [q_1, q_2, q_3, q_0]^\mathsf{T}$ is

$$\mathbf{R}[\bar{\boldsymbol{q}}] = [\boldsymbol{r}_1\, \boldsymbol{r}_2\, \boldsymbol{r}_3], \quad \boldsymbol{r}_1 = \begin{bmatrix} q_0^2 + q_1^2 - q_2^2 - q_3^2 \\ 2(q_1q_2 - q_0q_3) \\ 2(q_1q_3 + q_0q_2) \end{bmatrix},$$
$$\boldsymbol{r}_2 = \begin{bmatrix} 2(q_1q_2 + q_0q_3) \\ q_0^2 - q_1^2 + q_2^2 - q_3^2 \\ 2(q_2q_3 - q_0q_1) \end{bmatrix},$$
$$\boldsymbol{r}_3 = \begin{bmatrix} 2(q_1q_3 - q_0q_2) \\ 2(q_2q_3 + q_0q_1) \\ q_0^2 - q_1^2 - q_2^2 + q_3^2 \end{bmatrix}.$$

The calculation of the discrete-time linearized INS state transition matrix $\boldsymbol{\Phi}_{\text{ins},n}$ and process noise covariance $\mathbf{Q}_{\text{ins},n}$ are performed using strapdown INS equations (2)–(3) resolved in an ECI frame as described in [50], [51]. The matrix $\boldsymbol{\Phi}_{\text{ins},n}$ is given by

$$\boldsymbol{\Phi}_{\text{ins},n}(i) = \begin{bmatrix} \mathbf{I}_{3\times3} & \mathbf{0}_{3\times3} & \mathbf{0}_{3\times3} & \boldsymbol{\Phi}_{\bar{\boldsymbol{q}}\boldsymbol{b}_{\text{gyr}},n} & \mathbf{0}_{3\times3} \\ \boldsymbol{\Phi}_{\boldsymbol{r}\bar{\boldsymbol{q}},n} & \mathbf{I}_{3\times3} & T\mathbf{I}_{3\times3} & \boldsymbol{\Phi}_{\boldsymbol{r}\boldsymbol{b}_{\text{gyr}},n} & \boldsymbol{\Phi}_{\boldsymbol{r}\boldsymbol{b}_{\text{acc}},n} \\ \boldsymbol{\Phi}_{\dot{\boldsymbol{r}}\bar{\boldsymbol{q}},n} & \mathbf{0}_{3\times3} & \mathbf{I}_{3\times3} & \boldsymbol{\Phi}_{\dot{\boldsymbol{r}}\boldsymbol{b}_{\text{gyr}},n} & \boldsymbol{\Phi}_{\dot{\boldsymbol{r}}\boldsymbol{b}_{\text{acc}},n} \\ \mathbf{0}_{3\times3} & \mathbf{0}_{3\times3} & \mathbf{0}_{3\times3} & \mathbf{I}_{3\times3} & \mathbf{0}_{3\times3} \\ \mathbf{0}_{3\times3} & \mathbf{0}_{3\times3} & \mathbf{0}_{3\times3} & \mathbf{0}_{3\times3} & \mathbf{I}_{3\times3} \end{bmatrix},$$
$$\boldsymbol{\Phi}_{\bar{\boldsymbol{q}}\boldsymbol{b}_{\text{gyr}},n} = -\frac{T}{2}\left[\hat{\mathbf{R}}_n^\mathsf{T}(i+1) + \hat{\mathbf{R}}_n^\mathsf{T}(i)\right],$$
$$\boldsymbol{\Phi}_{\dot{\boldsymbol{r}}\bar{\boldsymbol{q}},n} = -\frac{T}{2}\left\lfloor\left[\hat{\boldsymbol{a}}_n(i) + \hat{\boldsymbol{a}}_n(i+1)\right]\times\right\rfloor, \quad \boldsymbol{\Phi}_{\boldsymbol{r}\bar{\boldsymbol{q}},n} = \frac{T}{2}\boldsymbol{\Phi}_{\dot{\boldsymbol{r}}\bar{\boldsymbol{q}},n},$$
$$\boldsymbol{\Phi}_{\dot{\boldsymbol{r}}\boldsymbol{b}_{\text{gyr}},n} = -\frac{T}{2}\left\lfloor\hat{\boldsymbol{a}}_n(i)\times\right\rfloor\boldsymbol{\Phi}_{\bar{\boldsymbol{q}}\boldsymbol{b}_{\text{gyr}},n}, \quad \boldsymbol{\Phi}_{\dot{\boldsymbol{r}}\boldsymbol{b}_{\text{acc}},n} = \boldsymbol{\Phi}_{\bar{\boldsymbol{q}}\boldsymbol{b}_{\text{gyr}},n},$$
$$\boldsymbol{\Phi}_{\boldsymbol{r}\boldsymbol{b}_{\text{gyr}},n} = \frac{T}{2}\boldsymbol{\Phi}_{\dot{\boldsymbol{r}}\boldsymbol{b}_{\text{gyr}},n}, \quad \boldsymbol{\Phi}_{\boldsymbol{r}\boldsymbol{b}_{\text{acc}},n} = \frac{T}{2}\boldsymbol{\Phi}_{\dot{\boldsymbol{r}}\boldsymbol{b}_{\text{acc}},n},$$

where $\hat{\mathbf{R}}_n(i) \triangleq \mathbf{R}\left[{}_g^{b_n}\hat{\bar{\boldsymbol{q}}}(i|j)\right]$ is the equivalent rotation matrix of ${}_g^{b_n}\hat{\bar{\boldsymbol{q}}}(i|j)$, which is the estimate of ${}_g^{b_n}\bar{\boldsymbol{q}}(i)$ using all measurements up to time-step j; $\hat{\boldsymbol{a}}_n(i) \triangleq \hat{\mathbf{R}}_n^\mathsf{T}(i)\left[{}^n\boldsymbol{a}_{\text{imu}}(i) - \hat{\boldsymbol{b}}_{\text{acc},n}(i|j)\right]$, where $\hat{\boldsymbol{b}}_{\text{acc},n}(i|j)$ is the estimate of $\boldsymbol{b}_{\text{acc},n}(i)$ using all measurements up to time-step j; and $\lfloor(\cdot)\times\rfloor$ is the skew-symmetric matrix obtained according to (16). The discrete-time linearized INS process noise covariance $\mathbf{Q}_{\text{ins},n}$ is given by

$$\mathbf{Q}_{\text{ins},n}(i) = \frac{T}{2}\boldsymbol{\Phi}_{\text{ins},n}(i)\mathbf{N}_{c,n}\boldsymbol{\Phi}_{\text{ins},n}^\mathsf{T}(i) + \mathbf{N}_{c,n},$$
$$\mathbf{N}_{c,n} = \text{diag}\left[\mathbf{S}_{\boldsymbol{n}_{\text{gyr}},n},\, \mathbf{0}_{3\times3},\, \mathbf{S}_{\boldsymbol{n}_{\text{acc}},n},\, \mathbf{S}_{\boldsymbol{w}_{\text{gyr}},n},\, \mathbf{S}_{\boldsymbol{w}_{\text{acc}},n}\right],$$

where $\mathbf{S}_{\boldsymbol{n}_{\text{gyr}},n} = T\mathbf{Q}_{\boldsymbol{n}_{\text{gyr}},n}$ and $\mathbf{S}_{\boldsymbol{n}_{\text{acc}},n} = T\mathbf{Q}_{\boldsymbol{n}_{\text{acc}},n}$ are the PSD matrices of the gyroscope's and accelerometer's random noise, respectively, and $\mathbf{S}_{\boldsymbol{w}_{\text{gyr}},n} = \mathbf{Q}_{\boldsymbol{w}_{\text{gyr}},n}/T$ and $\mathbf{S}_{\boldsymbol{w}_{\text{acc}},n} = \mathbf{Q}_{\boldsymbol{w}_{\text{acc}},n}/T$ are the PSD matrices of the gyroscope's and accelerometer's bias variation, respectively, which may be derived from values obtained from IMU specification sheets.

Acknowledgment

The authors would like to thank Jesse Garcia for his help with data collection.

References

[1] *40+ Corporations Working on Autonomous Vehicles*, CB Insights, New York, NY, USA, 2019.
[2] D. Gettinger, *Summary of Drone Spending in the FY 2019 Defense Budget Request*. New York, NY, USA: Center for Study Drone at Bard College, 2019.
[3] J. Du and M. J. Barth, "Next-generation automated vehicle location systems: Positioning at the lane level," *IEEE Trans. Intell. Transp. Syst.*, vol. 9, no. 1, pp. 48–57, Mar. 2008.
[4] Y. I. Jenie, E.-J. van Kampen, J. Ellerbroek, and J. M. Hoekstra, "Safety assessment of a UAV CDR system in high density airspace using Monte Carlo simulations," *IEEE Trans. Intell. Transp. Syst.*, vol. 19, no. 8, pp. 2686–2695, Aug. 2018.
[5] I. Miller and M. Campbell, "Sensitivity analysis of a tightly-coupled GPS/INS system for autonomous navigation," *IEEE Trans. Aerosp. Electron. Syst*, vol. 48, no. 2, pp. 1115–1135, Apr. 2012.
[6] I. Skog and P. Handel, "In-car positioning and navigation technologies—A survey," *IEEE Trans. Intell. Transp. Syst.*, vol. 10, no. 1, pp. 4–21, Mar. 2009.
[7] A. Soloviev, "Tight coupling of GPS, INS, and laser for urban navigation," *IEEE Trans. Aerosp. Electron. Syst.*, vol. 46, no. 4, pp. 1731–1746, Nov. 2010.
[8] A. Hata and D. Wolf, "Feature detection for vehicle localization in urban environments using a multilayer LIDAR," *IEEE Trans. Intell. Transp. Syst.*, vol. 17, no. 2, pp. 420–429, Feb. 2016.
[9] W. Wen, G. Zhang, and L.-T. Hsu, "Object-detection-aided GNSS and its integration with lidar in highly urbanized areas," *IEEE Intell. Transp. Syst. Mag.*, vol. 12, no. 3, pp. 53–69, Fall 2020.
[10] C. N. Taylor, M. J. Veth, J. F. Raquet, and M. M. Miller, "Comparison of two image and inertial sensor fusion techniques for navigation in unmapped environments," *IEEE Trans. Aerosp. Electron. Syst.*, vol. 47, no. 2, pp. 946–958, Apr. 2011.
[11] C. Rose, J. Britt, J. Allen, and D. Bevly, "An integrated vehicle navigation system utilizing lane-detection and lateral position estimation systems in difficult environments for GPS," *IEEE Trans. Intell. Transp. Syst.*, vol. 15, no. 6, pp. 2615–2629, Dec. 2014.
[12] K. Kozak and M. Alban, "Ranger: A ground-facing camera-based localization system for ground vehicles," in *Proc. IEEE/ION Position, Location Navigat. Symp. (PLANS)*, Apr. 2016, pp. 170–178.
[13] R. Toledo-Moreo, D. Betaille, and F. Peyret, "Lane-level integrity provision for navigation and map matching with GNSS, dead reckoning, and enhanced maps," *IEEE Trans. Intell. Transp. Syst.*, vol. 11, no. 1, pp. 100–112, Mar. 2010.
[14] Z. Kassas, M. Maaref, J. Morales, J. Khalife, and K. Shamei, "Robust vehicular localization and map matching in urban environments through IMU, GNSS, and cellular signals," *IEEE Intell. Transp. Syst. Mag.*, vol. 12, no. 3, pp. 36–52, Jun. 2020.
[15] M. Rohani, D. Gingras, and D. Gruyer, "A novel approach for improved vehicular positioning using cooperative map matching and dynamic base station DGPS concept," *IEEE Trans. Intell. Transp. Syst.*, vol. 17, no. 1, pp. 230–239, Jan. 2016.

[16] A. Hansen *et al.*, "Complementary PNT and GPS backup technologies demonstration report: Sections 1 through 10," Nat. Transp. Syst. Center, Cambridge, MA, USA, Tech. Rep. DOT-VNTSC-20-07, 2021.

[17] Z. Kassas, J. Khalife, A. Abdallah, and C. Lee, "I am not afraid of the jammer: Navigating with signals of opportunity in GPS-denied environments," in *Proc. ION GNSS Conf.*, 2020, pp. 1566–1585.

[18] J. McEllroy, "Navigation using signals of opportunity in the AM transmission band," M.S. thesis, School Eng., Air Force Inst. Technol., Wright-Patterson Air Force Base, OH, USA, 2006.

[19] S.-H. Fang, J.-C. Chen, H.-R. Huang, and T.-N. Lin, "Is FM a RF-based positioning solution in a metropolitan-scale environment? A probabilistic approach with radio measurements analysis," *IEEE Trans. Broadcast.*, vol. 55, no. 3, pp. 577–588, Sep. 2009.

[20] C. Yang and T. Nguyen, "Tracking and relative positioning with mixed signals of opportunity," *Navigation*, vol. 62, no. 4, pp. 291–311, Dec. 2015.

[21] J. Khalife and Z. Kassas, "Navigation with cellular CDMA signals—Part II: Performance analysis and experimental results," *IEEE Trans. Signal Process.*, vol. 66, no. 8, pp. 2204–2218, Apr. 2018.

[22] J. A. del Peral-Rosado, J. A. Lopez-Salcedo, F. Zanier, and G. Seco-Granados, "Position accuracy of joint time-delay and channel estimators in LTE networks," *IEEE Access*, vol. 6, pp. 25185–25199, 2018.

[23] K. Shamaei and Z. Kassas, "LTE receiver design and multipath analysis for navigation in urban environments," *Navigat., J. Inst. Navigat.*, vol. 65, no. 4, pp. 655–675, Dec. 2018.

[24] P. Thevenon *et al.*, "Positioning using mobile TV based on the DVB-SH standard," *Navigation*, vol. 58, no. 2, pp. 71–90, Jun. 2011.

[25] J. Yang, X. Wang, M. J. Rahman, S. I. Park, H. M. Kim, and Y. Wu, "A new positioning system using DVB-T2 transmitter signature waveforms in single frequency networks," *IEEE Trans. Broadcast.*, vol. 58, no. 3, pp. 347–359, Sep. 2012.

[26] T. G. R. Reid, A. M. Neish, T. Walter, and P. K. Enge, "Broadband LEO constellations for navigation," *Navigation*, vol. 65, no. 2, pp. 205–220, Jun. 2018.

[27] Z. Kassas, J. Morales, and J. Khalife, "New-age satellite-based navigation–STAN: Simultaneous tracking and navigation with LEO satellite signals," *Inside GNSS Mag.*, vol. 14, no. 4, pp. 56–65, 2019.

[28] A. Abdallah and Z. Kassas, "Deep learning-aided spatial discrimination for multipath mitigation," in *Proc. IEEE/ION Position, Location Navigat. Symp. (PLANS)*, Apr. 2020, pp. 1324–1335.

[29] Z. Kassas, J. Morales, K. Shamaei, and J. Khalife, "LTE steers UAV," *GPS World Mag.*, vol. 28, no. 4, pp. 18–25, Apr. 2017.

[30] J. Morales and Z. Kassas, "Tightly-coupled inertial navigation system with signals of opportunity aiding," *IEEE Trans. Aerosp. Electron. Syst.*, vol. 57, no. 3, pp. 1930–1948, Jun. 2021.

[31] J. Morales, J. Khalife, and Z. Kassas, "GNSS vertical dilution of precision reduction using terrestrial signals of opportunity," in *Proc. ION Int. Tech. Meeting Conf.*, Jan. 2016, pp. 664–669.

[32] Z. Kassas and T. Humphreys, "Observability analysis of collaborative opportunistic navigation with pseudorange measurements," *IEEE Trans. Intell. Transp. Syst.*, vol. 15, no. 1, pp. 260–273, Feb. 2014.

[33] C. Yang and A. Soloviev, "Simultaneous localization and mapping of emitting radio sources-SLAMERS," in *Proc. ION GNSS Conf.*, Sep. 2015, pp. 2343–2354.

[34] H. Durrant-Whyte and T. Bailey, "Simultaneous localization and mapping: Part I," *IEEE Robot. Autom. Mag.*, vol. 13, no. 2, pp. 99–110, Jun. 2006.

[35] J. Morales and Z. Kassas, "Distributed signals of opportunity aided inertial navigation with intermittent communication," in *Proc. ION GNSS Conf.*, Sep. 2017, pp. 2519–2530.

[36] D.-H. Shin and T.-K. Sung, "Comparisons of error characteristics between TOA and TDOA positioning," *IEEE Trans. Aerosp. Electron. Syst.*, vol. 38, no. 1, pp. 307–311, Jan. 2002.

[37] T. Sathyan, M. Hedley, and M. Mallick, "An analysis of the error characteristics of two time of arrival localization techniques," in *Proc. 13th Int. Conf. Inf. Fusion*, Jul. 2010, pp. 1–7.

[38] R. Kaune, "Accuracy studies for TDOA and TOA localization," in *Proc. Int. Conf. Inf. Fusion*, Jul. 2012, pp. 408–415.

[39] J. Morales and Z. Kassas, "Information fusion strategies for collaborative radio SLAM," in *Proc. IEEE/ION Position Location Navigat. Symp.*, Apr. 2018, pp. 1445–1454.

[40] Y. Wang and X. R. Li, "Distributed estimation fusion with unavailable cross-correlation," *IEEE Trans. Aerosp. Electron. Syst.*, vol. 48, no. 1, pp. 259–278, Jan. 2012.

[41] L. Carrillo-Arce, E. Nerurkar, J. Gordillo, and S. Roumeliotis, "Decentralized multi-robot cooperative localization using covariance intersection," in *Proc. IEEE/RSJ Int. Conf. Intell. Robots Syst.*, 2013, pp. 1412–1417.

[42] N. Alam, A. Kealy, and A. G. Dempster, "Cooperative inertial navigation for GNSS-challenged vehicular environments," *IEEE Trans. Intell. Transp. Syst.*, vol. 14, no. 3, pp. 1370–1379, Sep. 2013.

[43] H. Li, F. Nashashibi, and M. Yang, "Split covariance intersection filter: Theory and its application to vehicle localization," *IEEE Trans. Intell. Transp. Syst.*, vol. 14, no. 4, pp. 1860–1871, Dec. 2013.

[44] H. Mokhtarzadeh and D. Gebre-Egziabher, "Cooperative inertial navigation," *Navigation*, vol. 61, no. 2, pp. 77–94, Jun. 2014.

[45] H. Mokhtarzadeh and D. Gebre-Egziabher, "Performance of networked dead reckoning navigation system," *IEEE Trans. Aerosp. Electron. Syst.*, vol. 52, no. 5, pp. 2539–2553, Oct. 2016.

[46] J. Zhu and S. S. Kia, "Cooperative localization under limited connectivity," *IEEE Trans. Robot.*, vol. 35, no. 6, pp. 1523–1530, Dec. 2019.

[47] A. Thompson, J. Moran, and G. Swenson, *Interferometry and Synthesis in Radio Astronomy*, 2nd ed. Hoboken, NJ, USA: Wiley, 2001.

[48] M. Shuster, "A survey of attitude representations," *The J. Astron. Sci.*, vol. 41, no. 4, pp. 439–517, Oct. 1993.

[49] M. Braasch, "Inertial navigation systems," in *Aerospace Navigation Systems*. Hoboken, NJ, USA: Wiley, 2016.

[50] J. Farrell and M. Barth, *The Global Positioning System and Inertial Navigation*. New York, NY, USA: McGraw-Hill, 1998.

[51] P. Groves, *Principles of GNSS, Inertial, and Multisensor Integrated Navigation Systems*, 2nd ed. Norwood, MA, USA: Artech House, 2013.

[52] J. Morales and Z. Kassas, "A low communication rate distributed inertial navigation architecture with cellular signal aiding," in *Proc. IEEE Veh. Technol. Conf.*, 2018, pp. 1–6.

[53] T. Amemiya, *Advanced Econometrics*. Cambridge, MA, USA: Harvard Univ. Press, 1985, p. 460.

[54] R. A. Snay and T. Soler, "Continuously operating reference station (CORS): History, applications, and future enhancements," *J. Surv. Eng.*, vol. 134, no. 4, pp. 95–104, 2008.

[55] M. S. Braasch and A. J. van Dierendonck, "GPS receiver architectures and measurements," *Proc. IEEE*, vol. 87, no. 1, pp. 48–64, Jan. 1999.

[56] S. Tay and J. Marais, "Weighting models for GPS pseudorange observations for land transportation in urban canyons," in *Proc. Eur. Workshop GNSS Signals Signal Process.*, Dec. 2013, pp. 1–4.

[57] J. C. Liberti and T. S. Rappaport, "A geometrically based model for line-of-sight multipath radio channels," in *Proc. Veh. Technol. Conf.*, vol. 2, Apr. 1996, pp. 844–848.

[58] M. Maaref and Z. Kassas, "Measurement characterization and autonomous outlier detection and exclusion for ground vehicle navigation with cellular signals," *IEEE Trans. Intell. Veh.*, vol. 5, no. 4, pp. 670–683, Dec. 2020.

[59] J. Khalife, K. Shamaei, and Z. Kassas, "Navigation with cellular CDMA signals—Part I: Signal modeling and software-defined receiver design," *IEEE Trans. Signal Process.*, vol. 66, no. 8, pp. 2191–2203, Apr. 2018.

[60] C. Gentner, T. Jost, W. Wang, S. Zhang, A. Dammann, and U.-C. Fiebig, "Multipath assisted positioning with simultaneous localization and mapping," *IEEE Trans. Wireless Commun.*, vol. 15, no. 9, pp. 6104–6117, Sep. 2016.

[61] A. Mannesson, M. A. Yaqoob, and B. Bernhardsson, "Tightly coupled positioning and multipath radio channel tracking," *IEEE Trans. Aerosp. Electron. Syst.*, vol. 52, no. 4, pp. 1522–1535, Aug. 2016.

[62] Y. Wang, Y. Wu, and Y. Shen, "Joint spatiotemporal multipath mitigation in large-scale array localization," *IEEE Trans. Signal Process.*, vol. 67, no. 3, pp. 783–797, Feb. 2019.

[63] P. Wang and Y. J. Morton, "Multipath estimating delay lock loop for LTE signal TOA estimation in indoor and urban environments," *IEEE Trans. Wireless Commun.*, vol. 19, no. 8, pp. 5518–5530, Aug. 2020.

[64] Z. Kassas and T. Humphreys, "Receding horizon trajectory optimization in opportunistic navigation environments," *IEEE Trans. Aerosp. Electron. Syst.*, vol. 51, no. 2, pp. 866–877, Apr. 2015.

[65] J. Morales and Z. Kassas, "Stochastic observability and uncertainty characterization in simultaneous receiver and transmitter localization," *IEEE Trans. Aerosp. Electron. Syst.*, vol. 55, no. 2, pp. 1021–1031, Apr. 2019.

[66] V. Indelman, S. Williams, M. Kaess, and F. Dellaert, "Information fusion in navigation systems via factor graph based incremental smoothing," *Robot. Auton. Syst.*, vol. 61, no. 8, pp. 721–738, Aug. 2013.

[67] W. Wen, Y. Kan, and L. Hsu, "Performance comparison of GNSS/INS integrations based on EKF and factor graph optimization," in *Proc. ION Int. Tech. Meeting*, Sep. 2019, pp. 3019–3032.

[68] D. Uciński, *Optimal Measurement Methods for Distributed Parameter System Identification*. Boca Raton, FL, USA: CRC Press, 2005.
[69] *QGP Supply GPS Active Antenna*. [Online]. Available: https://qgpsupply.com/index.php/2017/10/20/waterproof-gps-active-antenna-28db-gain/
[70] (2020). *Ettus Research Tri-Band Antenna*. [Online]. Available: https://www.ettus.com/all-products/vert400
[71] K. Pesyna, Z. Kassas, J. Bhatti, and T. Humphreys, "Tightly-coupled opportunistic navigation for deep urban and indoor positioning," in *Proc. ION GNSS Conf.*, Sep. 2011, pp. 3605–3617.
[72] Z. Kassas, V. Ghadiok, and T. Humphreys, "Adaptive estimation of signals of opportunity," in *Proc. ION GNSS Conf.*, Sep. 2014, pp. 1679–1689.

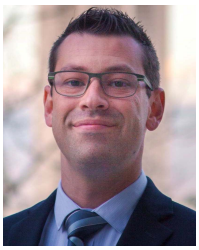

Joshua J. Morales (Member, IEEE) received the B.S. degree (Hons.) in electrical engineering from the University of California, Riverside, CA, USA, and the Ph.D. degree in electrical engineering and computer science from the University of California, Irvine (UCI), Irvine, CA, USA. He is currently a Principal with StarNav LLC. Previously, he was a member of the Autonomous Systems Perception, Intelligence, and Navigation (ASPIN) Laboratory, UCI. His research interests include estimation theory, navigation systems, autonomous vehicles, and cyber-physical systems. In 2016, he was a recipient of the Honorable Mention from the National Science Foundation (NSF). In 2018, he received the National Center for Sustainable Transportation (NCST) Outstanding Graduate Student of the Year Award.

Joe J. Khalife (Student Member, IEEE) received the B.E. degree in electrical engineering and the M.S. degree in computer engineering from Lebanese American University (LAU). He is currently pursuing the Ph.D. degree with the University of California, Irvine. From 2012 to 2015, he was a Research Assistant at LAU. He is currently a member of the Autonomous Systems Perception, Intelligence, and Navigation (ASPIN) Laboratory. His research interests include opportunistic navigation, autonomous vehicles, and software-defined radio.

Zaher (Zak) M. Kassas (Senior Member, IEEE) received the B.E. degree in electrical engineering from Lebanese American University, the M.S. degree in electrical and computer engineering from The Ohio State University, and the M.S.E. degree in aerospace engineering and the Ph.D. degree in electrical and computer engineering from The University of Texas at Austin. He is currently an Associate Professor with the University of California, Irvine, and the Director of the Autonomous Systems Perception, Intelligence, and Navigation (ASPIN) Laboratory. He is also the Director of the U.S. Department of Transportation, Center for Automated Vehicles Research with Multimodal AssurEd Navigation (CARMEN), focusing on navigation resiliency and security of highly automated transportation systems. His research interests include cyber-physical systems, estimation theory, navigation systems, autonomous vehicles, and intelligent transportation systems. He is a recipient of the 2018 National Science Foundation (NSF) Faculty Early Career Development Program (CAREER) Award, the 2019 Office of Naval Research (ONR) Young Investigator Program (YIP) Award, the 2018 IEEE Walter Fried Award, the 2018 Institute of Navigation (ION) Samuel Burka Award, and the 2019 ION Col. Thomas Thurlow Award. He is a Senior Editor for the IEEE TRANSACTIONS ON INTELLIGENT VEHICLES and an Associate Editor of the IEEE TRANSACTIONS ON AEROSPACE AND ELECTRONIC SYSTEMS and the IEEE TRANSACTIONS ON INTELLIGENT TRANSPORTATION SYSTEMS.